Development of Carbon Nitride based Heterostructure for Environmental Remediation

Dissertation submitted to
Visvesvaraya National Institute of Technology, Nagpur
in partial fulfilment of the requirements for the award of
the degree

Master of Science
in
Chemistry

by

TANMAY GUPTA (MS23CHM007)

under the guidance of

Prof. Suresh S. Umare

Department of Chemistry
Visvesvaraya National Institute of Technology
Nagpur 440010 (India)

May 2025

©Visvesvaraya National Institute of Technology (VNIT) 2025

Visvesvaraya National Institute of Technology, Nagpur

Declaration

I, Tanmay Gupta hereby declare that this dissertation titled **"Development of Carbon Nitride based Heterostructure for Environmental Remediation"** is carried out by me in the **Department of Chemistry** of Visvesvaraya National Institute of Technology, Nagpur. The work is original and has not been submitted earlier whole or in part for the award of any degree/diploma at this or any other Institution / University.

Tanmay Gupta
Date:

Certificate

This is to certify that the dissertation titled **"Development of Carbon Nitride based Heterostructure for Environmental Remediation"** is submitted by **Tanmay Gupta** in partial fulfilment of the requirements for the award of the degree of **Master of Science in Chemistry**, VNIT Nagpur. The work is comprehensive, complete and fit for final evaluation.

Prof. Suresh S. Umare
Professor, Dept, VNIT, Nagpur

Head, Department of Chemistry
VNIT, Nagpur
Date:

DEPARTMENT OF CHEMISTRY

VISVESVARYA NATIONAL INSTITUTE OF TECHNOLOGY, NAGPUR

Non-Plagiarism Certificate

Certified that M.Sc. Dissertation titled “Development of g-C3N4 based Photocatalyst for Degradation of Pollutants” submitted by Tanmay Gupta Enrollment No. MS23CHM007 ID No. 30261 has been checked for plagiarism using TURNITIN software and the overlap is found within prescribed limits. A summary of the report is given below:

Tanmay Gupta
MS23CHM007
Id No: 30261

Prof. S.S. Umare
Department of Chemistry
VNIT, Nagpur

Acknowledgement

I would like to express my deepest gratitude to my supervisor, **Prof. Suresh S. Umare**, Department of Chemistry, for his encouragement and patience during the course of my M.Sc. project. I am very thankful to his tutelage and disciplinary inspiration which has helped me to improve my personal skills. I extend my thanks to the Department of Chemistry, for providing the necessary facilities to undertake the project efficiently.

I convey my sincere gratitude to **Mr. Swapnil Sarkar**, Doctoral Fellow at VNIT, Nagpur for his constant support and guidance. I am also thankful to **Mr. Pritam Ramteke, Ms. Ruchika, Mrs. Renuka and Ms. Anjali**, Doctoral Fellow at VNIT, Nagpur for their tremendous mentorship in the lab and my friend **Miss Palak** for her help and cheerful atmosphere in the lab.

Finally, I would like to thank my family and friends whose constant support and blessings helped me throughout the project.

Tanmay Gupta
(MS23CHM007)

ABSTRACT

Development of Graphitic Carbon Nitride based Heterostructure for Environmental Remediation

Tanmay Gupta (MS23CHM007) and Suresh S. Umare
Materials and Catalysis Laboratory, Department of Chemistry, Visvesvaraya National Institute of Technology (VNIT), Nagpur, India

In recent years, environmental pollution has become a major concern due to its severe threat to ecosystems. Moreover, the growing contamination of water sources has led to an increasing demand for clean and fresh water. Consequently, water pollution has emerged as a significant issue that is expected to intensify over time. In response, visible light-active semiconductors, such as Graphitic Carbon Nitride (g-C_3N_4), have garnered significant attention due to its metal-free composition, ability to absorb visible light (with a band gap of 2.7 eV), and excellent thermal stability. However, its limited surface area and high recombination rate of photoexcitons hinder its overall photocatalytic efficiency.

Our research focuses on the fabrication of a heterostructure by combining C_3N_7 with g-C_3N_4 in order to overcome the limitations. The synthesis of the C_3N_7/g-C_3N_4 heterostructure was achieved through the thermal polymerization method. To characterize the heterostructure, we used various techniques, including p-XRD (To examine the phase formation), FTIR (To analyse the molecular structure and bonding), UV-DRS (To study the optical response), TGA (To evaluate the thermal stability), BET (To determine the surface area and porosity), FESEM (To investigate the surface morphology), TEM (To examine the internal structure and composition). Furthermore, the photocatalytic activity of C_3N_7/g-C_3N_4 heterostructure was evaluated by testing its ability towards degradation of Rhodamine B (RhB) dye and to reduce Cr(VI) to Cr(III). The optimised heterostructure (5C_3N_7/g-C_3N_4) demonstrated significantly high photocatalytic activity compared to pure g-C_3N_4, C_3N_7 and other heterostructures, owing to improved visible light absorption, a larger surface area, and reduced recombination rates of photoexcited electron-hole pairs which collectively boost the material's photocatalytic efficiency.

List of Figures

Fig. no.	Figures	Page no.
	Chapter 1	
1.1	Classification of Dyes	2
1.2	Molecular configuration of Rhodamine B dye	3
1.3	Catalytic effect shown by Potential Energy Diagram	5
1.4	Semiconductor based Photocatalytic degradation pathways	7
1.5	Illustration of Photogenerated Charge Carrier Pathways	8
1.6	Electronic Band Structure of Semiconductors	9
1.7	Carbon Nitride structure elucidated by Liebig	11
1.8	Synthesis of g-C_3N_4 using various precursors	11
1.9	g-C_3N_4 frameworks: a) Triazine, b) Tris-s-triazine	12
1.10	Polymeric C_3N_7 framework	14
	Chapter 2	
2.1	Representation of Bragg's diffraction in a crystal, illustrating two beams with identical wavelength and phase.	20
	Chapter 3	
3.1	Powder X-ray diffraction pattern of g-C_3N_4, C_3N_7 and its composites	28
3.2	(a) UV-Vis DRS Spectrum and (b) Kubelka-Munk plots of as prepared caralysts	29

3.3	Fourier Transform Infrared (FT-IR) Spectrum Analysis of g-C3N4, C3N7 and its composites	30-31
3.4	(a) N_2 adsorption-desorption isotherm and (b) Pore size distribution of g-C_3N_4, C_3N_7 and 5C_3N_7/g-C_3N_4 composite	32
3.5	SEM Images	33
3.6	TEM Images	34
3.7	Plausible Mechanism for photodegradation of RhB	35
3.8	Photocatalytic RhB degradation performance of g-C_3N_4, C_3N_7 and its composites	36
3.9	(a) Photocatalytic Dye Degradation by 5C_3N_7/g-C_3N_4 in presence of scavengers, and (b) Corresponding Percentage Degradation in presence of quenchers	37
3.10	Recyclability assessment of 5C_3N_7/g-C_3N_4 catalyst for degradation of RhB	38
3.11	Photocatalytic reduction of Cr(VI) to Cr(III)	39

List of Tables

Table No.	Title	Page No.
3.1	Textural Parameters of g-C_3N_4, C_3N_7 and 5C_3N_7/g-C_3N_4 composite	33

Nomenclature

Abbreviation	Full Form
ROS	Reactive Oxygen Species
AOP	Advanced Oxidation Process
VB	Valence Band
CB	Conduction Band
h^+	Hole
e^-	Electron
TCH	Tetracycline Hydrochloride
RhB	Rhodamine B
g-C_3N_4	Graphitic Carbon Nitride
XRD	X-Ray Diffraction
UV-Vis DRS	UV-Visible Diffusive Reflectance Spectra
TGA	Thermogravimetric Analysis
FTIR	Fourier-Transform Infrared Spectroscopy
SEM	Scanning Electron Microscope
TEM	Transmission Electron Microscope
PL	Photoluminescence

Contents

S. no.	Contents	Page no.
	Chapter 1	
	Introduction	
1.1	**Environmental Sustainability**	**1**
1.2	**Organic Dye induced pollution**	**1-2**
1.2.1	Classification of Dyes	2
1.2.2	Dye selected for investigation: Rhodamine B	3
1.3	**Various Waste Water Remediation Technique**	**3-5**
1.3.1	Chemical Precipitation	3-4
1.3.2	Reverse Osmosis	4
1.3.3	Adsorption	4
1.3.4	Ion Exchange	4-5
1.4	**Catalysis**	**5-6**
1.4.1	Homogeneous Catalysis	6
1.4.2	Heterogeneous Catalysis	6
1.5	**Photocatalysis**	**6-10**
1.5.1	Mechanism of Photocatalysis	7-8
1.5.2	Various Semiconducting materials used for Photocatalysis	8-10
	(a) Metal Oxides	
	(b) Metal Sulphides and Selenides	
	(c) Carbon based materials	
1.6	**Graphitic Carbon Nitride**	**10-14**
1.6.1	Advantages of g-C_3N_4	12-13

1,6.2	Limitations of g-C_3N_4	13
1.6.3	Strategies to Overcome the Limitations of g-C_3N_4	13
1.6.4	Heterostructure Engineering	13-14
1.7	**Polymeric C_3N_7**	**14**
1.8	**Aims and Objectives**	**15**
1.9	**Thesis Overview**	**15**
1.10	**References**	**16-18**
	Chapter 2	
	Synthesis and Characterization Methods	
2.1	**Chemicals**	**19**
2.2	**Methods of Preparation**	**19**
2.2.1	Synthesis Method of bulk g-C_3N_4	19
2.2.2	Synthesis Method of C_3N_7	19
2.2.3	Synthesis method of C_3N_7/g-C_3N_4 Composite	19
2.3	**Characterization Techniques**	**22-25**
2.3.1	Powder X-ray Diffraction (XRD)	20-21
2.3.2	UV-Visible Spectroscopy	21
2.3.3	UV-Vis Diffuse Reflectance Spectroscopy (UV-Vis DRS)	21-22
2.3.4	Fourier Transform Infrared Spectroscopy (FT-IR)	22
2.3.5	Surface Area and Pore Size Distribution	22-23
2.3.6	Evaluation of Photocatalytic Activity	23-24
2.3.7	Field Emission Scanning Electron Microscopy (FE-SEM)	24-25
2.3.8	Transmission Electron Microscopy (TEM)	25

2.4	**References**	**26-27**
	Chapter 3	
	Results and Discussion	
3.1	**Crystal Structure, Optical Properties, and Structural Examination**	**28-29**
3.2	**Optical Property and Charge Separation Efficiency**	**29-30**
3.3	**FT-IR (Fourier Transform Infrared) Spectroscopy**	**30-31**
3.4	**Surface Area and Pore Size Distribution**	**32-33**
3.5	**FE-SEM Images**	**34-35**
3.6	**TEM Images**	**35-36**
3.7	**Evaluation of Photocatalytic Degradation Behaviour and Mechanism**	**36**
3.7.1	Rhodamine B Degradation	37-38
3.7.1.1	Quenchers Study	38-39
3.7.1.2	Recyclability	39
3.8	**Photocatalytic Reduction of Cr(VI) to Cr(III)**	**40**
3.9	**References**	**41**
	Chapter 4	
	Summary and Conclusion	
4.1	**Summary and Conclusion**	**42**
4.2	**Future Aspects**	**42**

CHAPTER 1

INTRODUCTION

This chapter opens by addressing the growing threats to environmental sustainability, followed by an exploration of semiconductor-mediated photocatalysis as a viable solution for pollution control, with a specific focus on metal-free g-C_3N_4 (a visible-light-active photocatalyst) emphasizing its strengths, limitations, and the strategies developed to enhance its performance. it also delves into the ecological risks posed by the release of carcinogenic dyes and pharmaceutical residues and their degradation. It concludes with the brief outline of the aims, objectives and scope of the current research.

1.1 Environmental Sustainability:

The world's most significant environmental concern is the dual threat of finite non-renewable energy resources and pervasive environmental pollution. The accelerating pace of urbanization, industrialization, and resource extraction has led to the rapid growth of toxic pollutants in the nature that disrupting the ecosystems and undermining the planet's ecological balance.[1]

Water is essential for life, playing a crucial role in regulating body temperature and facilitating various metabolic processes. It aids in synthesizing and structuring cellular components, transporting nutrients, and supporting overall bodily functions. However, water contamination disrupts these processes, leading to severe health issues. Shockingly, approximately two million tons of wastewater from sewage, industry, and agriculture are released into water bodies daily, as reported by the UN in 2003.[2] As a universal solvent, water becomes a breeding ground for infections when contaminated. The World Health Organization (WHO) reveals that:

- Water-Borne Diseases: 80% of diseases are linked to contaminated water.
- Global Health Concerns: Many countries' drinking water fails to meet WHO standards.
- Mortality Rate: About 3.1% of deaths are attributed to consuming poor-quality water.

1.2 Organic Dye induced pollution:

Organic dyes find broad application in various industries like textiles, paper production, food processing, plastics, printing, leather, and pharmaceuticals. Their large-scale manufacturing and widespread use have led to the contamination of water bodies and soil. These dyes, especially synthetic ones, pose serious ecological risks owing to their long-

lasting presence and toxicity. In marine or freshwater environment, they can adversely affect both human and animal health.[7]

Moreover, many dyes possess carcinogenic and mutagenic properties, posing serious threats to humans, microorganisms, and both terrestrial and aquatic ecosystems. Due to these hazardous effects, there is a growing global focus on developing effective methods for the removal and degradation of these dyes to mitigate their environmental impact.

1.2.1 Classification of Dyes:

Dyes can be classified based on various criteria such as their chemical structure, colour, and method of application. One of the most widely accepted systems for classifying dyes is the Colour Index (CI). A primary method of classification distinguishes dyes according to their origin—either natural or synthetic.

Another approach classifies dyes based on their behaviour in aqueous solutions, specifically their ability to dissociate into ions. From this perspective, dyes are categorized as either cationic (basic dyes), that exhibits a positive charge, or anionic (acidic dyes), that exhibits a negative charge. This ionic nature plays a crucial role in determining how dyes interact with substrates and how they are selected for degradation processes. Notably, the choice of dye also depends significantly on its environmental impact, particularly the toxicity associated with certain colours.

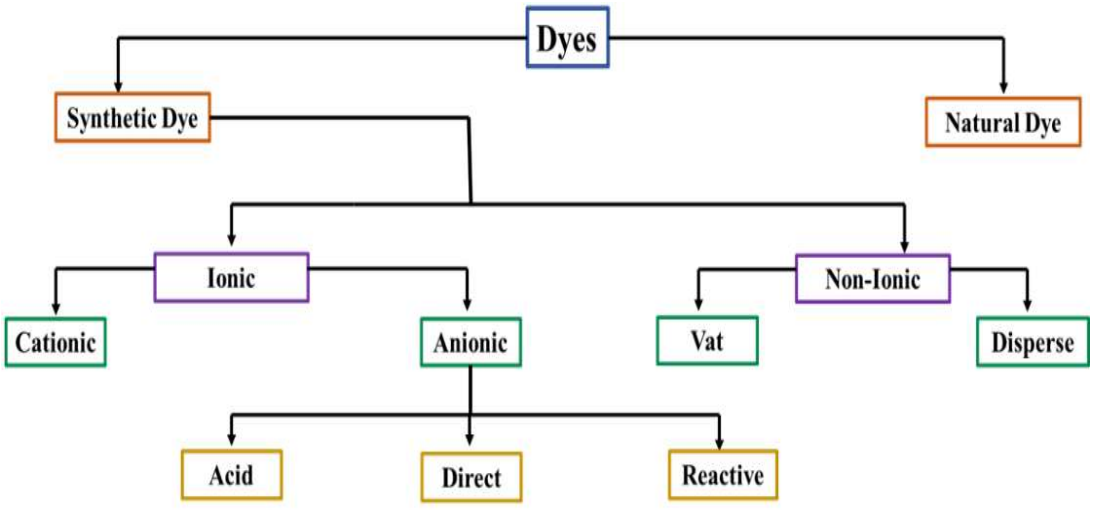

Figure 1.1 Classification of Dyes

1.2.2 Dye selected for investigation: Rhodamine B:

Rhodamine B (RhB) is a synthetic xanthene dye in the form of an organic chloride salt, commonly used in a range of industrial applications including textiles, paper, paints, and leather. Due to its bright fluorescence and water solubility, it is often applied in printing and dyeing processes.

Despite its usefulness, Rhodamine B poses serious environmental and health risks. It is toxic to humans and aquatic organisms, with potential effects such as eye damage, nausea, headaches, skin irritation, and respiratory problems upon inhalation, ingestion, or skin contact.[8] Owing to these hazardous properties, Rhodamine B has been selected as a model pollutant in photocatalytic degradation studies.

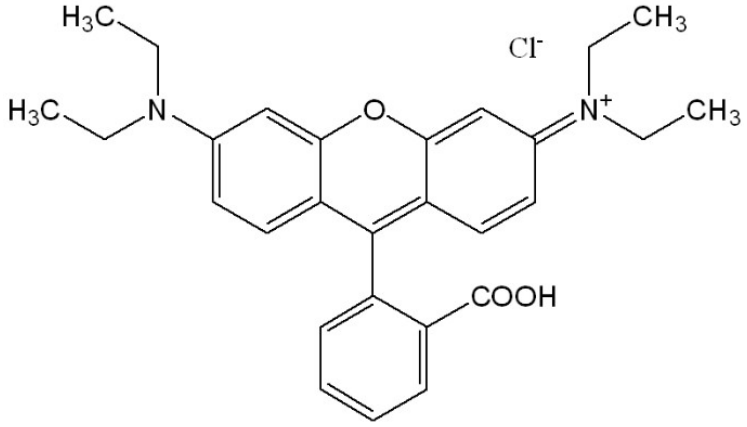

Figure 1.2 Molecular configuration of Rhodamine B dye

1.3 Various Waste Water Remediation Technique:

Several traditional methods have been widely utilized to manage and remediate contaminated water. The following sub-sections summarize some of the key techniques:

1.3.1 Chemical Precipitation:

Chemical precipitation is widely used for removing heavy metals, phosphates, and emulsified oils and greases from industrial wastewater. This method works by adding specific chemicals that react with dissolved contaminants, transforming them into insoluble solids. These precipitated solids can then be separated from the liquid phase through filtration or sedimentation.[9]

Limitations: The technique often requires large quantities of chemicals and generates significant sludge that must be managed. Moreover, its efficiency diminishes when metal ions are present at very low concentrations.

1.3.2 Reverse Osmosis:

Reverse osmosis is a pressure-driven filtration process that utilizes a semipermeable membrane to separate larger particles and dissolved salts from water. These membranes are constructed with charged functional groups that hinder the passage of ions or molecules with similar charges.[2] When pressure is applied, only small molecules like water are allowed to pass, while larger particles and ions are retained.

Limitations: It requires a considerable volume of water to function effectively, and in the process, it removes essential minerals from drinking water.

1.3.3 Adsorption:

Adsorption involves the attachment of dissolved pollutants onto the surface of solid materials. It is governed by surface energy and is effective for both organic and inorganic contaminant removal.[10] Commonly employed adsorbents include activated carbon, metal oxides, chitosan, and natural minerals like zeolite. These materials offer large surface areas and high affinity for various contaminants.

Limitations: This method lacks specificity, and the adsorbent surfaces can rapidly become saturated. Additionally, clogging issues are frequently observed, reducing overall efficiency.

1.3.4 Ion Exchange:

The ion exchange process chemically replaces harmful dissolved ions in water with beneficial alternatives. The exchange occurs between a liquid phase (usually water) and a solid medium such as a resin or zeolite. This method is often employed in water softening processes to reduce the concentrations of calcium and magnesium ions.

Limitations: This method is not effective in removing microbial contaminants. It is also expensive and requires large columns or reactors, making it space- and resource-intensive.

Due to the many shortcomings of conventional water treatment methods, alternative approaches are gaining significant interest. Among these, **photocatalysis** has emerged as a particularly promising technique. As an advanced oxidation process, it offers considerable advantages over traditional methods, including efficiency, environmental friendliness, and minimal secondary pollution. A key benefit of photocatalysis is that the catalysts used can be recovered and reused, making the process both sustainable and cost-effective. These qualities have made it a focal point of recent research in the field of wastewater treatment.

1.4 Catalysis:

Catalysis plays a vital role on a global scale, especially in improving air quality by reducing harmful pollutants. It requires the introduction of a catalyst to a chemical reaction, which accelerates the reaction rate without being consumed or altered in the process.[11]

The presence of a catalyst reduces the activation energy required for the reaction to take place (as shown in Figure 1.4). This reduction in activation energy allows the reaction to take place rapidly and efficiently, often in lower temperature conditions.

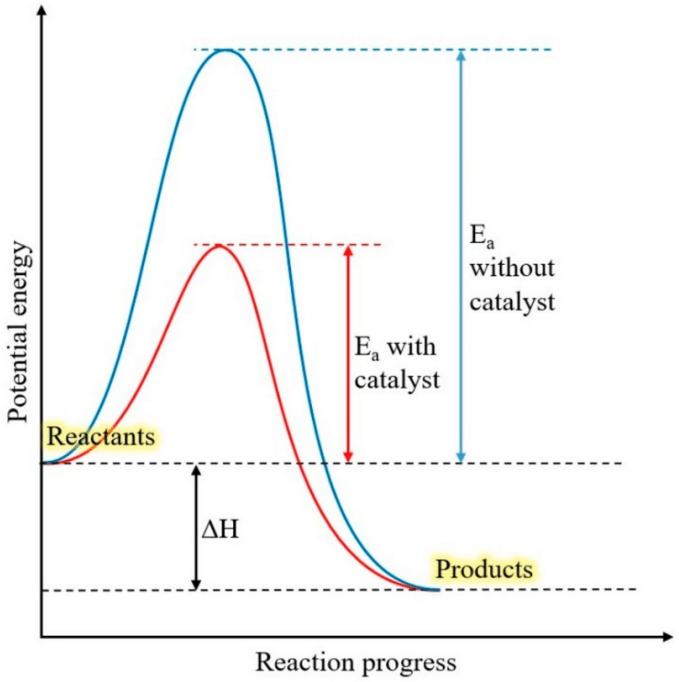

Figure 1.3 Catalytic effect shown by Potential Energy Diagram

Catalytic processes are generally categorized based on the physical phase of the catalyst and reactants involved:

1.4.1 Homogeneous Catalysis:

In homogeneous catalysis, both the catalyst and reactants exist in the same phase commonly in a liquid solution.[12] This uniformity allows for efficient interaction between the catalyst and the reacting species, often resulting in highly effective reactions. However, one major drawback of this method is the difficulty in recovering and reusing the catalyst, making it non-recyclable.

1.4.2 Heterogeneous Catalysis:

Heterogeneous catalysis refers to catalytic processes where the catalyst and the reactants exist in different phases. Typically, the catalyst is in a solid state, while the reactants are in liquid or gaseous phases. The reaction generally occurs through the adsorption of reactant molecules onto the catalyst's surface. This mechanism is often explained by the lock-and-key model, which suggests that the substrate fits precisely into the active sites of the catalyst.[13]

1.5 Photocatalysis:

Photocatalysis is a catalytic process driven by light energy, where one or more reactive species undergo a chemical transformation upon exposure to light. This approach commonly employs semiconductor materials as photocatalysts due to their ability to absorb light in the ultraviolet or visible range of the electromagnetic spectrum. When these semiconductors are illuminated with light energy equal to or greater than their band gap, electrons in the valence band (VB) become excited and transition to the conduction band (CB), leaving behind positive holes in the VB. These charge carriers excited electrons and holes initiate oxidation-reduction reactions that produce reactive oxygen species (ROS), including hydroxyl radicals (OH•), which are instrumental in breaking down pollutants.[14]

For the photocatalytic reaction to be effective, the band energy levels associated with conduction and valence bands must be properly aligned with the redox potentials of the reactive species involved. Efficient charge transfer requires the conduction band to lie at a more negative potential and the valence band at a more positive potential than the redox

potentials of the target species. Photocatalysis presents a promising solution for the degradation of various environmental pollutants, offering a sustainable approach to address some of today's most pressing environmental concerns.

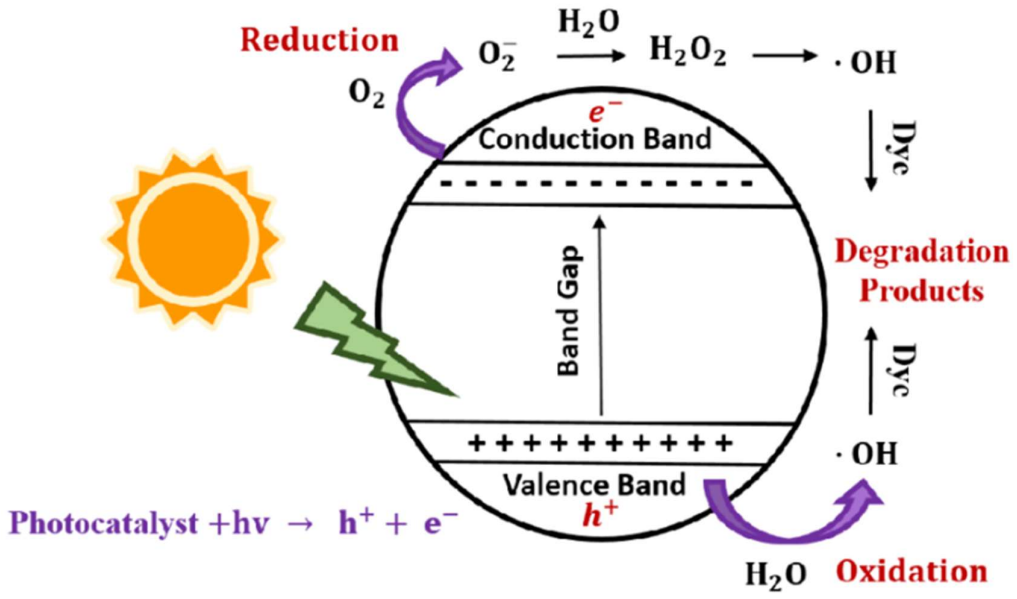

Figure 1.4 Semiconductor based Photocatalytic degradation pathway

1.5.1 Mechanism of Photocatalysis:

When exposed to light, a photocatalyst produces electrons (e^-) occupying the conduction band and holes (h^+) residing in the valence band. These charge carriers can follow several different pathways on the catalyst's surface:

1. Absorption of photons by the semiconductor

2. Separation of the generated charges

3. Oxidation reactions

4. Reduction reactions

5. Possible recombination of charges at the surface

6. Recombination within the bulk (volume) of the material

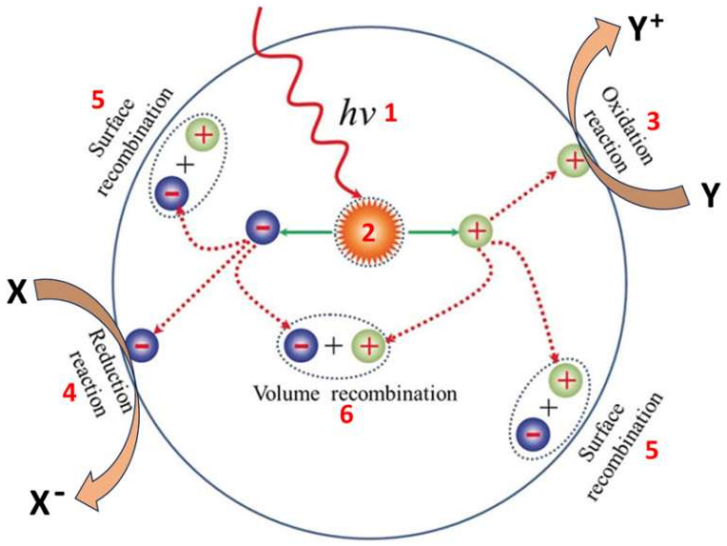

Figure 1.5 Illustration of Photogenerated Charge Carrier Pathways

Molecules can undergo either oxidation or reduction (corresponding to steps 3 and 4) depending on whether they receive a hole or an electron. Recombination of charges can happen at the surface (step 5), or deeper within the semiconductor material (step 6), when the electrons and holes meet and neutralize each other.[15]

1.5.2 Various Semiconducting materials used for Photocatalysis:

- **Metal based Photocatalysts:**

Metal Oxides:

Metal oxides constitute a significant class of semiconductor materials extensively employed in wastewater treatment applications. Their widespread use is primarily attributed to their excellent chemical stability, suitable optical band gap, and efficient photo-excitations under light irradiation.[16] Common examples of metal oxides used as photocatalysts include titanium dioxide (TiO_2), zirconium dioxide (ZrO_2), tungsten trioxide (WO_3), ferric oxide (Fe_3O_4), and zinc oxide (ZnO). The photocatalytic performance of these materials is largely influenced by their physicochemical properties, including particle size, morphology, and chemical composition.[17]

Despite their advantages, most metal oxides possess wide band gaps, rendering them to exhibits activity exclusively under UV irradiation. Given that UV radiation constitutes merely 3–5% of the complete solar radiation spectrum, the utilization of these materials

under natural sunlight is limited. For instance, a typical UV-responsive photocatalyst with a band gap somewhere around 3.2 eV absorbs only in the UV region of the electromagnetic spectrum, which demands higher energy and thus reduces energy efficiency.

Moreover, many metal oxides are susceptible to photo-corrosion and leaching when exposed to prolonged light irradiation, further limiting their practical applicability. To address these drawbacks, various modification strategies have been developed, including elemental doping, heterostructure engineering, and copolymerization techniques. These approaches are aimed at narrowing the band gap and improving the overall photocatalytic efficiency of metal oxide-based materials.

Metal Selenides and Sulphides:

Photocatalysts in this category typically include metal chalcogenides such as ZnS, CdS, and MoS_2, as well as metal selenides like CdSe and ZnSe. These materials are widely employed in photocatalytic water purification processes. Their popularity stems from features like a low band gap, absorption within the visible region of the electromagnetic spectrum (EMS), and appropriate redox potentials. However, despite these advantages, these materials are susceptible to photodegradation under light exposure, which limits their direct use in photocatalysis.[18]

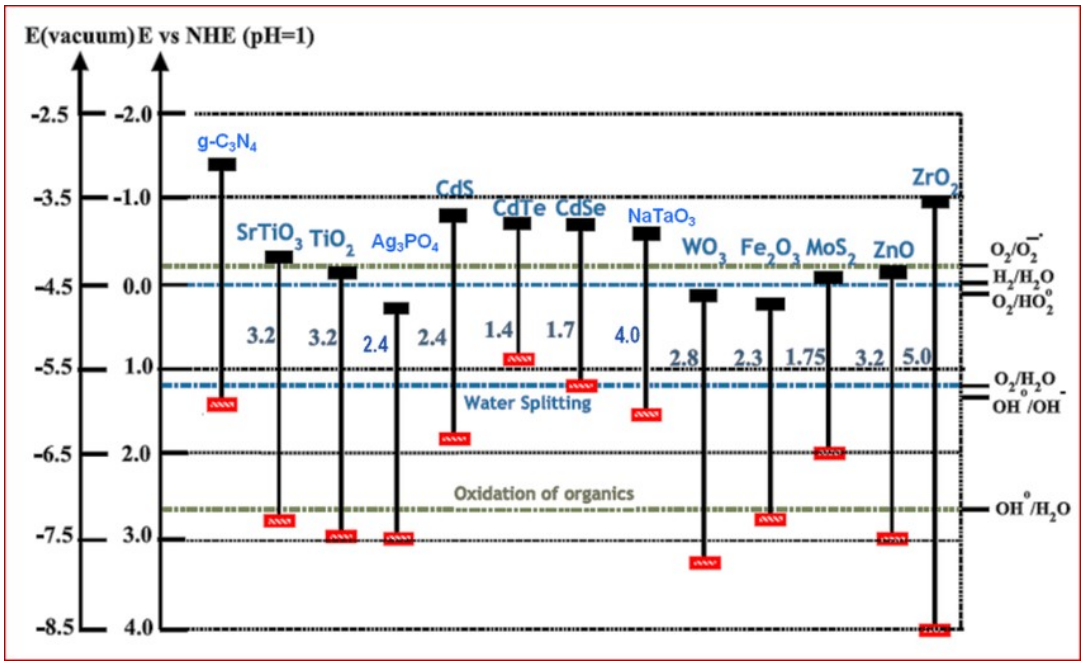

Figure 1.6 Electronic Band Structure of Semiconductors

- **Metal free Photocatalysts:**

In recent years, metal-free photocatalysts have been extensively studied due to their eco-friendliness, cost-effectiveness, and stability under light irradiation. These materials provide a sustainable substitute for traditional metal-based semiconductors, eliminating concerns related to metal toxicity, scarcity, and leaching during photocatalytic processes.

Carbon-based materials represent a major class of metal-free photocatalysts due to their distinctive structural, optical, and electronic characteristics, materials such as carbon nanotubes (CNTs), graphene, graphene oxide (GO), carbon dots, and graphitic carbon nitride (g-C_3N_4) have demonstrated strong visible light absorption and exceptional charge carrier mobility. These characteristics contribute to efficient light harvesting and improved spatial separation of photo-induced electrons and holes, each of which are essential for enhancing photocatalytic performance.[19]

A significant milestone in the fabrication of purely organic or carbon-based photocatalysts was the discovery of graphitic carbon nitride (g-C_3N_4) in 2009. This polymeric material, composed solely of carbon and nitrogen, has since emerged as a benchmark photocatalyst because of its ideally positioned band gap (~2.7 eV), high chemical stability, and ease of synthesis from abundant precursors like melamine or urea. g-C_3N_4 has been widely explored for applications such as hydrogen generation, pollutant degradation, and CO_2 reduction.

Unlike metal-based photocatalysts, metal-free systems are inherently resistant to photo corrosion and do not suffer from metal ion leaching, making them more durable under prolonged irradiation. Additionally, these materials can be further engineered through doping, surface modification, or the formation of heterostructures to optimize their band edge position and improve photocatalytic activity.

1.6 Graphitic Carbon Nitride:

The origin of graphitic carbon nitride (g-C_3N_4) dates back to 1834 when Berzelius synthesized a compound called "melon," a linear polymer consisting of triazine units linked through secondary nitrogen atoms. Later, Liebig named this compound.[20] Over time, various types of carbon nitride structures have been discovered, including α-C_3N_4, β-C_3N_4, γ-C_3N_4, pseudo cubic C_3N_4, and cubic-C_3N_4. Among these, graphitic carbon

nitride (g-C_3N_4) stands out as the most thermodynamically stable form under ambient conditions. It is also known for its rich surface chemistry, making it suitable for diverse applications.[21]

Graphitic carbon nitride is a polymeric, heterocyclic compound composed of sp^2 hybridized carbon and nitrogen atoms arranged in an alternating pattern. The structure features layers of heptazine or triazine units, which provide thermal and chemical stability. Typically, polymeric g-C_3N_4 appears as a yellowish powder with a nitrogen-to-carbon (N/C) ratio of about 1.33. The conduction and valence band edge positions are around -1.1 eV and +1.6 eV, respectively, resulting in a band gap of around 2.7 eV. This enables efficient absorption of visible light, particularly around the 460 nm wavelength.[22]

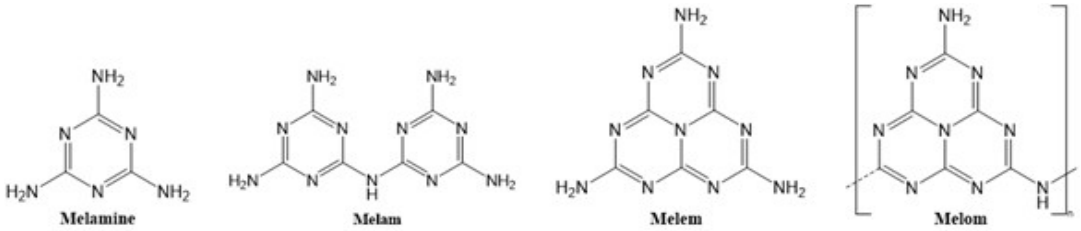

Figure 1.7 Carbon Nitride structure elucidated by Liebig

Polymeric g-C_3N_4 is typically synthesized through thermal polymerization, where nitrogen- and carbon-rich precursors like urea, melamine, or cyanamide are exposed to calcination process in a muffle furnace at approximately 550°C.[23]

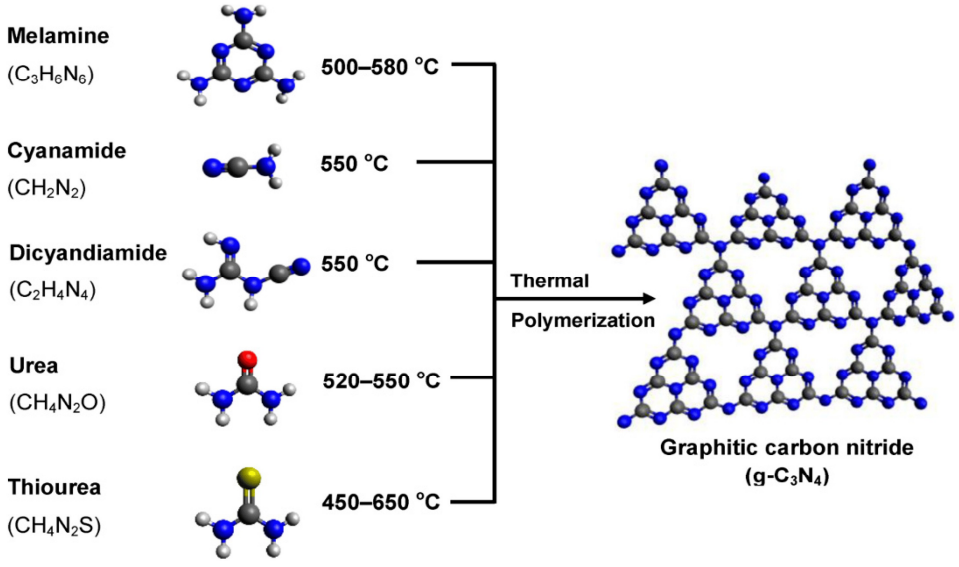

Figure 1.8 Synthesis of g-C_3N_4 using various precursors

"Depending on its repeating structural unit, polymeric g-C_3N_4 is generally classified into two types: triazine-based and tri-s-triazine (heptazine) based structures, as depicted in the figure."

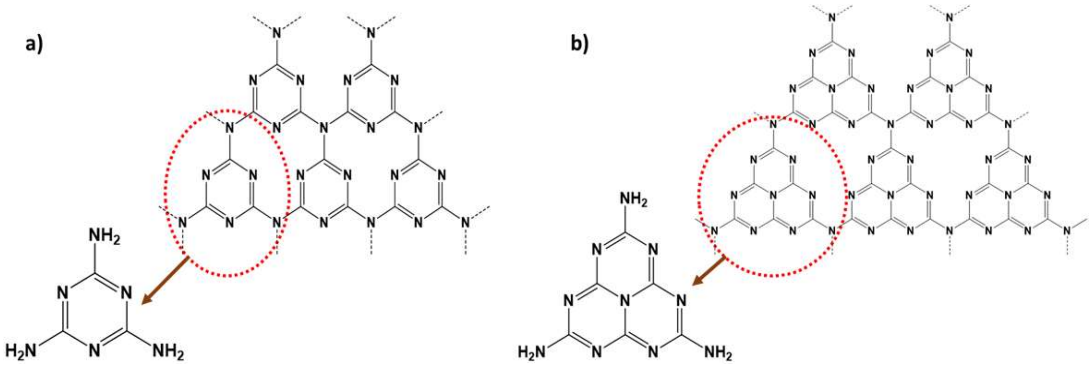

Figure 1.9 g-C_3N_4 frameworks: a) Triazine, b) Tris-s-triazine

1.6.1 Advantages of g-C_3N_4:

- **Metal-Free Composition:** Graphitic carbon nitride (g-C_3N_4) is composed exclusively of carbon and nitrogen, with no involvement of metal atoms. This metal-free nature offers strong resistance to photocorrosion and eliminates the risk of metal ion leaching, making it highly stable and environmentally friendly.
- **High Thermal Stability:** g-C_3N_4 exhibits exceptional thermal durability, maintaining its structure at temperatures up to 550°C. This property makes it well-suited for high-temperature operations in various catalytic and material science applications.
- **Narrow Band Gap:** With a band gap of approximately 2.7 eV, g-C_3N_4 can absorb visible light effectively, enabling its activation under natural sunlight toward energy-related and ecological applications.
- **Visible-Light Responsiveness:** Its ability to be activated by visible light makes g-C_3N_4 a promising material for solar-driven photocatalysis and optoelectronic devices.
- **Non-Toxic and Environmentally Safe:** Being inherently non-toxic, g-C_3N_4 poses minimal environmental risks, supporting its use in sustainable and green technologies.

- **Chemical Inertness:** Due to its planar, polymeric structure, g-C_3N_4 exhibits high chemical stability, showing limited reactivity with a diverse set of organic substances.
- **Poor Solubility in Organic Solvents:** The material's low solubility in both organic and inorganic solvents contributes to its robustness in harsh chemical environments.
- **Cost-Effective Synthesis:** g-C_3N_4 can be synthesized from low-cost, widely available precursors such as urea and melamine, making it an economically viable material for large-scale applications.

1.6.2 Limitations of g-C_3N_4:

- **Restricted Light Penetration:** Due to its stacked, layered structure, the diffusion and penetration of light into the interior layers of g-C_3N_4 is limited. This structural constraint hampers the material's light-harvesting efficiency, thereby reducing its photocatalytic performance.
- **High Recombination Rate of Charge Carriers:** The photo-induced charge carriers (electrons and holes) in g-C_3N_4 tend to recombine rapidly, resulting in the loss of reactive species and diminishing the material's catalytic efficiency.
- **Limited Surface Area:** The tightly packed layers reduce the accessible surface area for reactions, thereby limiting the count of active sites present for catalysis.

1.6.3 Strategies to Overcome the Limitations of g-C_3N_4:

To address the above limitations and enhance the photocatalytic efficiency of g-C_3N_4, various modification techniques have been developed. These include elemental doping with metals or non-metals, surface functionalization, nano-structuring, sensitization, and heterostructure formation. Among these, heterostructure engineering has emerged as one of the most efficient approaches for improving electron-hole pair separation and enhancing light absorption.[20]

1.6.3.1 Heterostructure Engineering:

Heterostructure design involves coupling two semiconductors to form an interface that facilitates directional transfer of charge carriers. This strategic alignment allows electrons to move from higher to lower potential and holes in the reverse direction, thereby

enhancing charge separation and reducing recombination rates.[24] Various types of heterojunctions such as Type I, Type II, Type III, p-n junctions, Schottky junctions, and Z-scheme systems have been studied for their potential to improve photocatalytic outcomes.[25] In addition to improving charge dynamics, heterostructure design can also positively influence material properties like surface area, optical absorption, and mechanical stability.

1.7 Polymeric C_3N_7:

Polymeric C_3N_7 is a lesser-known polymorph of carbon nitride that features a nitrogen-to-carbon atomic ratio greater than 2. This high nitrogen content lends the material strong basicity and favourable optoelectronic characteristics. Typically orange in appearance, C_3N_7 exhibits a broad band gap of around 3.2 eV. Like g-C_3N_4, it is synthesized through a thermal polymerization route, though it requires relatively lower temperatures for processing.

Structurally, C_3N_7 consists of tetrazine and triazole units linked via nitrogen-nitrogen bonds, forming a robust framework (as depicted in Figure 1.11).[26] In terms of electronic structure, C_3N_7 exhibits a conduction band (CB) edge of –0.87 eV and a valence band (VB) edge of +2.18 eV. Comparatively, g-C_3N_4 has a CB edge at –1.1 eV and a VB edge at +1.6 eV. The alignment of their respective energy bands enables the construction of an efficient Type II heterojunction, facilitating better charge separation and enhanced photocatalytic activity when the two materials are combined.[27]

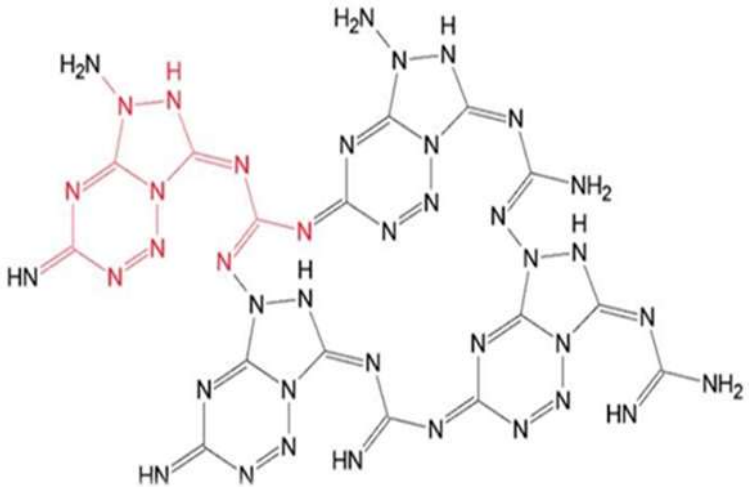

Figure:1.10 Polymeric C_3N_7 framework

1.8 Aims and Objectives:

The central objectives of the present research work are:

- To synthesize graphitic carbon nitride-based materials, specifically g-C_3N_4, C_3N_7, and their composite forms.
- To perform comprehensive characterization of the synthesized g-C_3N_4, C_3N_7 and g-C_3N_4/C_3N_7 composites.
- To explore the photocatalytic capabilities of the g-C_3N_4/C_3N_7 composites for the degradation of RhB and reduction of Cr (VI).

1.9 Thesis Overview:

This thesis is structured into four main chapters, covering the introduction, experimental methods, results with discussions, and the concluding remarks along with future outlook.

Chapter 1: Introduction: This chapter introduces the concept of photocatalysis, providing its definition, historical background, and a discussion of existing semiconductor photocatalysts utilized for degradation purposes.

Chapter 2: Synthesis and Characterization Methods: This section describes the materials employed throughout the research, the synthesis procedures developed for material preparation, and the characterization techniques adopted to investigate their structural and functional properties.

Chapter 3: Results and Discussion: In this chapter, the structural, optical, and functional attributes of the as-synthesized materials are analysed. It also includes an evaluation of their photocatalytic capabilities, particularly focusing on the degradation of pharmaceutical compounds and dyes.

Chapter 4: Summary, Conclusions, and Future Prospects: This final chapter provides a succinct summary of the research findings, draws major conclusions from the study, and discusses potential future research directions that could extend the work further.

1.10 References

1. Liu, C.; Dai, H.; Tan, C.; Pan, Q.; Hu, F.; Peng, X., Photo-Fenton degradation of tetracycline over Z-scheme Fe-g-C3N4/Bi2WO6 heterojunctions: Mechanism insight, degradation pathways and DFT calculation. Applied Catalysis B: Environmental **2022,** 310, 121326.
2. Sharma, S.; Bhattacharya, A., Drinking water contamination and treatment techniques. Applied water science **2017,** 7 (3), 1043-1067.
3. Kenawy, E.-R.; Bowlin, G. L.; Mansfield, K.; Layman, J.; Simpson, D. G.; Sanders, E. H.; Wnek, G. E., Release of tetracycline hydrochloride from electrospun poly (ethylene-co-vinylacetate), poly (lactic acid), and a blend. Journal of controlled release **2002,** 81 (1-2), 57-64.
4. Kraemer, S. A.; Ramachandran, A.; Perron, G. G., Antibiotic pollution in the environment: from microbial ecology to public policy. Microorganisms **2019,** 7 (6), 180.
5. Olusegun, S. J.; Larrea, G.; Osial, M.; Jackowska, K.; Krysinski, P., Photocatalytic degradation of antibiotics by superparamagnetic iron oxide nanoparticles: Tetracycline case. Catalysts **2021,** 11 (10), 1243.
6. Ahmad, F.; Zhu, D.; Sun, J., Environmental fate of tetracycline antibiotics: degradation pathway mechanisms, challenges, and perspectives. Environmental Sciences Europe **2021,** 33 (1), 64.
7. Tkaczyk, A.; Mitrowska, K.; Posyniak, A., Synthetic organic dyes as contaminants of the aquatic environment and their implications for ecosystems: A review. Science of the total environment **2020,** 717, 137222.
8. Zhuang, J.; Dai, W.; Tian, Q.; Li, Z.; Xie, L.; Wang, J.; Liu, P.; Shi, X.; Wang, D., Photocatalytic degradation of RhB over TiO2 bilayer films: effect of defects and their location. Langmuir **2010,** 26 (12), 9686-9694.
9. EPA, U., Wastewater Technology Fact Sheet Chemical Precipitation. Office of Water and Watersheds, Washington DC: United States Environmental Protection Agency. doi: EPA **2000.**
10. Rashed, M. N., Adsorption technique for the removal of organic pollutants from water and wastewater. Organic pollutants-monitoring, risk and treatment **2013,** 7, 167-194.

11. Inglezakis, V.; Poulopoulos, S., Adsorption, ion exchange and catalysis. Elsevier: 2006; Vol. 3.
12. Van Leeuwen, P. W., Homogeneous catalysis: understanding the art. Springer Science & Business Media: 2006.
13. Bond, G. C., Heterogeneous catalysis. **1987.**
14. Mills, A.; Le Hunte, S., An overview of semiconductor photocatalysis. Journal of photochemistry and photobiology A: Chemistry **1997,** 108 (1), 1-35.
15. Pan, H.; Heagy, M. D., Photons to formate: a review on photocatalytic reduction of CO2 to formic acid. Nanomaterials **2020,** 10 (12), 2422.
16. Hua, M.; Zhang, S.; Pan, B.; Zhang, W.; Lv, L.; Zhang, Q., Heavy metal removal from water/wastewater by nanosized metal oxides: a review. Journal of hazardous materials **2012,** 211, 317-331.
17. Khan, M. M.; Adil, S. F.; Al-Mayouf, A., Metal oxides as photocatalysts. Elsevier: 2015; Vol. 19, pp 462-464.
18. Henshaw, G.; Parkin, I.; Shaw, G., Convenient, low-energy synthesis of metal sulfides and selenides: PbS, Ag2E, ZnE, CuE (E=S, Se). Chemical Communications **1996,** 10, 1095-1096.
19. Syed, N.; Huang, J.; Feng, Y.; Wang, X.; Cao, L., Carbon-based nanomaterials via heterojunction serving as photocatalyst. Frontiers in chemistry **2019,** 7, 713.
20. Ong, W.-J.; Tan, L.-L.; Ng, Y. H.; Yong, S.-T.; Chai, S.-P., Graphitic carbon nitride (g-C3N4)-based photocatalysts for artificial photosynthesis and environmental remediation: are we a step closer to achieving sustainability? Chemical reviews **2016,** 116 (12), 7159-7329.
21. Zhu, J.; Xiao, P.; Li, H.; Carabineiro, S. A., Graphitic carbon nitride: synthesis, properties, and applications in catalysis. ACS applied materials & interfaces **2014,** 6 (19), 16449-16465.
22. Liu, J.; Zhang, T.; Wang, Z.; Dawson, G.; Chen, W., Simple pyrolysis of urea into graphitic carbon nitride with recyclable adsorption and photocatalytic activity. Journal of Materials Chemistry **2011,** 21 (38), 14398-14401.
23. Wang, X.; Blechert, S.; Antonietti, M., Polymeric graphitic carbon nitride for heterogeneous photocatalysis. ACS Catalysis **2012,** 2 (8), 1596-1606.
24. Low, J.; Yu, J.; Jaroniec, M.; Wageh, S.; Al-Ghamdi, A. A., Heterojunction photocatalysts. Advanced materials **2017,** 29 (20), 1601694.

25. Ren, Y.; Zeng, D.; Ong, W.-J., Interfacial engineering of graphitic carbon nitride (g-C3N4)-based metal sulfide heterojunction photocatalysts for energy conversion: a review. Chinese Journal of Catalysis **2019,** 40 (3), 289-319.
26. Vidyasagar, D.; Bhoyar, T.; Singh, G.; Vinu, A., Recent progress in polymorphs of carbon nitride: Synthesis, properties, and their applications. Macromolecular Rapid Communications **2021,** 42 (7), 2000676.
27. Kim, I. Y.; Kim, S.; Premkumar, S.; Yang, J. H.; Umapathy, S.; Vinu, A., Thermodynamically stable mesoporous C3N7 and C3N6 with ordered structure and their excellent performance for oxygen reduction reaction. Small **2020,** 16 (12), 1903572.

CHAPTER 2

SYNTHESIS AND CHARACTERIZATION METHODS

This chapter outlines the materials and methodologies employed for synthesizing g-C_3N_4, C_3N_7, and their composites. It also provides a foundational overview of the characterization techniques used, explaining their principles and areas of application.

2.1 Chemicals:

Melamine was sourced from Sigma-Aldrich (USA), while 5-amino-1H-tetrazole (5-ATTZ) was obtained from Tokyo Chemical Industry (TCI, Japan). All chemicals were used directly without any additional purification steps. Deionized water was employed in the preparation of every solution.

2.2 Methods of Preparation:

2.2.1 Synthesis Method of bulk g-C_3N_4:

Bulk g-C_3N_4 was produced through the thermal polycondensation of melamine.[1] Specifically, melamine was enclosed within a closed silica crucible and heated at 550°C for 2 hours in a muffle furnace. Once cooled to ambient temperature, the resulting yellow material was ground into a fine powder.

2.2.2 Synthesis Method of C_3N_7:

C_3N_7 was synthesized by thermally condensing 5 grams of 5-ATTZ. This reaction took place in a silica crucible at 250°C for 4 hours in an air furnace. The resulting orange-brown solid was left to cool naturally to ambient temperature and then ground into a fine powder.[2]

2.2.3 Synthesis method of C_3N_7/g-C_3N_4 Composite:

To prepare the C_3N_7/g-C_3N_4 composite, a specified amount (x mg) of 5-ATTZ was mixed with 500 grams of bulk g-C_3N_4. Subsequently, the mixture was heated at 250°C for 2 hours in a silica crucible in an air furnace. Upon cooling to room temperature, the orange-yellow product was crushed into a fine powder. The resulting composite was denoted as xC_3N_7/g-C_3N_4, **(**where x = 2.5, 5, and 10 mg of 5ATTZ used during synthesis of the composites).

2.3 Characterization Techniques:

2.3.1 Powder X-ray Diffraction (p-XRD):

Powder X-ray Diffraction (p-XRD) is a widely used analytical procedure for analysing the crystal structure, interplanar spacing, and lattice parameters of powdered solid materials.[3] In this technique, a specimen is subjected to an X-ray beam, and the resulting diffraction pattern is recorded at different incident angles. The observed patterns and intensities are influenced by both the angle of incidence and the strength of the diffracted rays. The setup generally includes a detector, collimators, and an X-ray source with a wavelength typically between 0.7 Å and 2 Å. XRD is fundamentally based on Bragg's Law, expressed by the equation:

$$n\lambda = 2d \sin\theta \quad \ldots\ldots\ldots\ldots\ldots\ldots \quad (1)$$

where:

d = distance between adjacent crystallographic planes,

θ = angle at which the X-ray strikes the crystal planes,

n = diffraction order (n = 1, 2, 3, ...),

λ = wavelength of the incident X-ray.

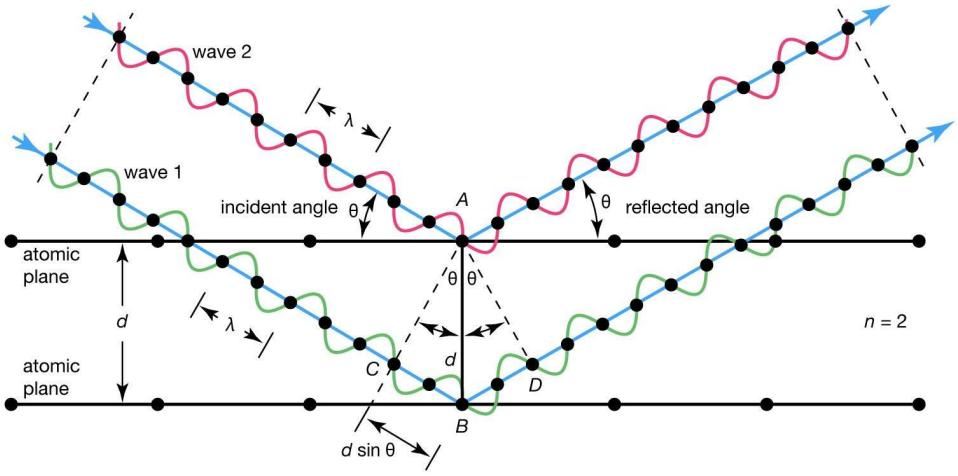

Figure 2.1 Representation of Bragg's diffraction in a crystal, illustrating two beams with identical wavelength and phase.

By plotting the diffracted ray intensity versus the diffraction angle (2θ), a unique pattern is generated, where each peak represents a particular set of crystal planes.

2.3.2 UV-Visible Spectroscopy:

UV-Visible (UV-Vis) spectroscopy is employed to analyse the absorption edge of a material. The technique is grounded in Beer-Lambert law, defines absorbance as being directly dependent on both the analyte concentration and the path length of the sample holder (cuvette).[4] This method enables the measurement of the amount of light absorbed at a specific wavelength based on the comparison between the incoming (I_0) and outgoing (I_t) light intensities. The absorbance (A) can be calculated using the formula:

$$\mathbf{A = -\log T = -\log (I_t / I_0) = \log (I_0 / I_t) = \varepsilon ct} \quad \text{..... (2)}$$

Where:

ε = molar absorptivity (extinction coefficient),

c = concentration of the analyte,

t = path length or thickness of the sample holder.

When UV-Visible radiation interacts with a sample, part of the light is absorbed while the rest passes through. The energy absorbed is influenced by electronic transitions, particularly between the HOMO (Highest Occupied Molecular Orbital) and LUMO (Lowest Unoccupied Molecular Orbital) levels, involving either π electrons or lone pair electrons. As the required transition energy increases, the absorption edge shifts toward shorter wavelengths, and vice versa.[5]

2.3.3 UV-Vis Diffuse Reflectance Spectroscopy (UV-Vis DRS):

UV-Vis DRS is commonly used to determine the optical bandgap of materials, especially semiconductors. Unlike standard UV-Vis, this technique focuses on reflected light instead of transmitted light. The analysis follows similar principles but uses reflectance data. Barium sulphate ($BaSO_4$) is typically used as a reference standard in this method.[6]

For UV-Vis DRS analysis (conducted using a UV 2600 Shimadzu spectrometer), the sample is exposed to light with wavelengths ranging from 200 to 700 nm. The data obtained is used to generate a Tauc plot or a Kubelka-Munk plot. By plotting $(\alpha hv)^{1/2}$

versus photon energy (hv), the bandgap energy can be derived. The linear region of $[F(R_\infty) hv]^{1/n}$ the plot is extrapolated to the x-axis at zero $F(R_\infty)$ which allows estimation of the optical bandgap of the sample.

2.3.4 Fourier Transform Infrared Spectroscopy (FT-IR):

Fourier Transform Infrared Spectroscopy (FTIR) is an essential analytical technique employed to identify functional groups within a sample. This method is based on the interaction of infrared radiation with molecular vibrations. Atoms within molecules or crystalline structures are bound by chemical bonds, and these structures exhibit characteristic vibrational motions dependent on the atomic mass and bond strength.

FTIR exploits the ability of infrared light to induce changes in the dipole moments of vibrating molecules, enabling detection of specific vibrational modes associated with functional groups. The infrared (IR) portion of the electromagnetic spectrum, typically spanning from 10^{12} to 10^{14} Hz, encompasses the frequencies at which these molecular vibrations occur.[7]

When the frequency of incident IR radiation matches the natural vibrational frequency of a bond, absorption takes place, resulting in a unique spectrum indicative of the sample's molecular composition. In this study, FTIR spectra were recorded using an IR Affinity-1 spectrophotometer (Shimadzu), with KBr pellets as the medium. Spectral data were collected in the range of 400–4000 cm^{-1}.

2.3.5 Surface Area and Pore Size Distribution:

The surface area and pore structure of materials are critical factors in determining their performance in heterogeneous catalysis and related applications. High surface area enhances the availability of active sites for chemical reactions, thereby improving catalytic efficiency. Consequently, characterization of surface area and porosity is vital for optimizing materials used in catalysis, adsorption, and other surface-mediated processes. Surface area and pore size characteristics are critical parameters in heterogeneous catalysis, as they influence access to active sites and thus impact catalytic efficiency. These properties can be determined by employing the Brunauer–Emmett–Teller (BET) theory.[8]

The principle underlying the BET method is based on the adsorption of a gas, typically nitrogen (N_2), onto the surface of a material with a known surface area. The degree of

adsorption depends on pressure and increases as pressure rises. Initially, gas molecules form a single layer on the surface, which eventually develops into multilayers as the relative vapor pressure continues to rise.[9]

Maximum adsorption is typically assumed to occur when a monolayer is formed. This phenomenon can be described using the Langmuir adsorption isotherm model, which is mathematically represented as:

$$C_e/q_e = 1/q_{max}\, K_L + C_e/q_{max} \quad \text{..... (3)}$$

Where:

q_{max} represents the maximum adsorption capacity (mg/g),

K_L is the Langmuir constant (L/g),

C_e/q_e is the specific sorption, and

C_e is the equilibrium concentration.

To conduct BET surface area and pore size analysis, a Quantachrome Nova touch 1 BET analyser was used.

2.3.6 Evaluation of Photocatalytic Activity:

The synthesized materials were evaluated for their photocatalytic performance based on their ability to degrade dye pollutants and reduction of Cr(VI). A specially designed photoreactor was used for this purpose, comprising a light source, a magnetic stirrer, a fan, and a sample container. A 250 mL glass beaker with a lid served as the sample vessel and was positioned over the magnetic stirrer. The entire setup was illuminated by seven fluorescent lamps (each 100 W) arranged uniformly around the sample. To prevent overheating, the chamber was equipped with two cooling fans.

The photocatalytic degradation of Rhodamine B (RhB) dye was investigated using 50 mg of the photocatalyst dispersed in 50 mL of a 30 mgL^{-1} dye solution. The suspension was first kept in the dark for 30 minutes to allow equilibrium between the dye and catalyst surfaces. Subsequently, the solution was irradiated with natural sunlight. At every 5 minutes of interval, approximately 5 mL of suspension was harvested and subjected to

centrifugation to remove turbidity. The clear supernatant was analysed using the UV-Vis spectrophotometer (UV 1800, Shimadzu) to evaluate dye degradation efficiency over time.

For the photocatalytic chromium (VI) reduction method, 20 ppm of chromium solution was prepared using potassium dichromate solution. 0.2M H_2SO_4 solution (250 mL) was prepared by dissolving 2.78 mL H_2SO_4 (18M) in 250 mL distilled water. The 1,5 diphenylcarbonohydrazide (DPC) solution was prepared by dissolving 0.125 gm DPC in 50 mL acetone.

The optimized catalyst $5C_3N_7$/g-C_3N_4, 50 mg catalyst was added to 50 mL $K_2Cr_2O_7$ solution (20 mg/L) and 19.7 mg citric acid were added in the above solution. The sample solution was stirred for 30 minutes in dark. After 30 minutes, the solution was stirred in visible light. Sample aliquots were filtered with a syringe filter and collected at the time interval of 5 minutes each.

Now, separate storage vials (glass vials) were taken and 7 mL H_2SO_4 (0.2M) was added in each vial. 0.2 mL of DPC solution was added into the storage glass vials (which already had 7 mL H_2SO_4) and shaken for proper mixing. 2mL of Chromium (VI) aliquots was added into the storage glass vials and the violet-coloured complex was formed. The vials were kept for 10 minutes for proper complex formation. Then, the absorbance data of the prepared solution was assessed using a (UV 1800 Shimadzu) UV-Vis spectrophotometer where absorbance values of each sample were recorded and the reduction efficiency was calculated by the formula:

$$\textbf{Degradation (\%)} = [C_0\text{-}C/C_0] * 100 \quad \textbf{(4)}$$

where C_0 represents the initial concentration of RhB.

C represents the concentration at a given time.

2.3.7 Field Emission Scanning Electron Microscopy (FE-SEM):

Field Emission Scanning Electron Microscopy (FE-SEM) was utilized to study the surface morphology and microstructural features of the synthesized photocatalyst. The high-resolution imaging capability of FE-SEM enabled a precise examination of particle size, shape, and surface topography. These structural characteristics are crucial because they directly influence the light-harvesting efficiency and the active surface area available for

photocatalytic reactions. The micrographs revealed a relatively uniform dispersion of nanoparticles, suggesting effective synthesis and minimal agglomeration.

Moreover, FE-SEM imaging allowed for the observation of porosity and surface roughness, which are important factors for enhancing photocatalytic performance. Rough and porous surfaces provide more active sites for light interaction and facilitate better adsorption of target pollutants. By correlating these morphological features with photocatalytic activity, FE-SEM offers a foundational understanding of how the physical structure supports or limits the functional behaviour of the catalyst under illumination.[10]

2.3.8 Transmission Electron Microscopy (TEM):

Transmission Electron Microscopy (TEM) was employed to gain deeper insights into the internal structure and nanoscale features of the photocatalyst. TEM analysis provided high-resolution images of individual particles, allowing the observation of crystallinity, particle boundaries, and internal lattice arrangements. The clear visibility of lattice fringes confirmed the crystalline nature of the material, while the measured interplanar spacings matched well with the expected values for specific crystal planes, validating the phase purity of the sample.[11]

Additionally, TEM offered evidence of any core-shell structures, heterojunctions, or embedded phases within the catalyst, which are particularly relevant for charge separation in photocatalytic systems. The presence of such nanostructures can significantly enhance photocatalytic efficiency by minimizing electron-hole recombination. Furthermore, Selected Area Electron Diffraction (SAED) patterns acquired during TEM analysis supported the crystalline findings and gave supplementary confirmation of the structural identity of the material. Overall, TEM plays a critical role in understanding the non-structural design that influences photocatalytic behaviour.

2.4 References:

1 Liu, J.; Zhang, T.; Wang, Z.; Dawson, G.; Chen, W., Simple pyrolysis of urea into graphitic carbon nitride with recyclable adsorption and photocatalytic activity. Journal of Materials Chemistry **2011,** 21 (38), 14398-14401.

2 Kim, I. Y.; Kim, S.; Premkumar, S.; Yang, J. H.; Umapathy, S.; Vinu, A., Thermodynamically stable mesoporous C3N7 and C3N6 with ordered structure and their excellent performance for oxygen reduction reaction. Small **2020,** 16 (12), 1903572.

3 Cullity, B.; Stock, S., Principles of X-ray diffraction. Rading, MA: Addison-Wesley **1978,** 90-95.

4 Dyamenahalli, K.; Famili, A.; Shandas, R., Characterization of shape-memory polymers for biomedical applications. In Shape memory polymers for biomedical applications, Elsevier: 2015; pp 35-63.

5 Smith, W. E., Some Spectroscopic and Chemical Studies and Their Application in Chemistry and Biology. University of Glasgow (United Kingdom): 1982.

6 Morozzi, P.; Ballarin, B.; Arcozzi, S.; Brattich, E.; Lucarelli, F.; Nava, S.; Gómez-Cascales, P. J.; Orza, J.; Tositti, L., Ultraviolet–Visible Diffuse Reflectance Spectroscopy (UV–Vis DRS), a rapid and non-destructive analytical tool for the identification of Saharan dust events in particulate matter filters. Atmospheric Environment **2021,** 252, 118297.

7 Titus, D.; Samuel, E. J. J.; Roopan, S. M., Nanoparticle characterization techniques. In Green synthesis, characterization and applications of nanoparticles, Elsevier: 2019; pp 303-319.

8 Thommes, M., Textural characterization of zeolites and ordered mesoporous materials by physical adsorption. Studies in surface science and catalysis **2007,** 495-523.

9 Walton, K. S.; Snurr, R. Q., Applicability of the BET method for determining surface areas of microporous metal–organic frameworks. Journal of the American Chemical Society **2007,** 129 (27), 8552-8556.

10 Chong, M. N.; Jin, B.; Chow, C. W. K.; Saint, C., Photocatalytic degradation of organic pollutants using TiO_2-based nanocomposites: A review. Water Research **2010,** 44 (10), 2997–3027.

11 Zhang, H.; Lv, X.; Li, Y.; Wang, Y.; Li, J., Enhanced photocatalytic activity of graphene oxide/TiO_2 composites for the decomposition of methylene blue under UV light irradiation. ACS Nano **2010,** 4 (1), 380–386.

CHAPTER 3

RESULTS AND DISCUSSION

This chapter presents the results and discussions derived from various experimental studies and characterization methods, including phase identification, surface area analysis, optical behaviour, thermal stability, and photocatalytic efficiency. It also provides a detailed explanation of the mechanism involved in the photodegradation of Tetracycline hydrochloride and Rhodamine B.

3.1 Crystal Structure, Optical Properties, and Structural Examination:

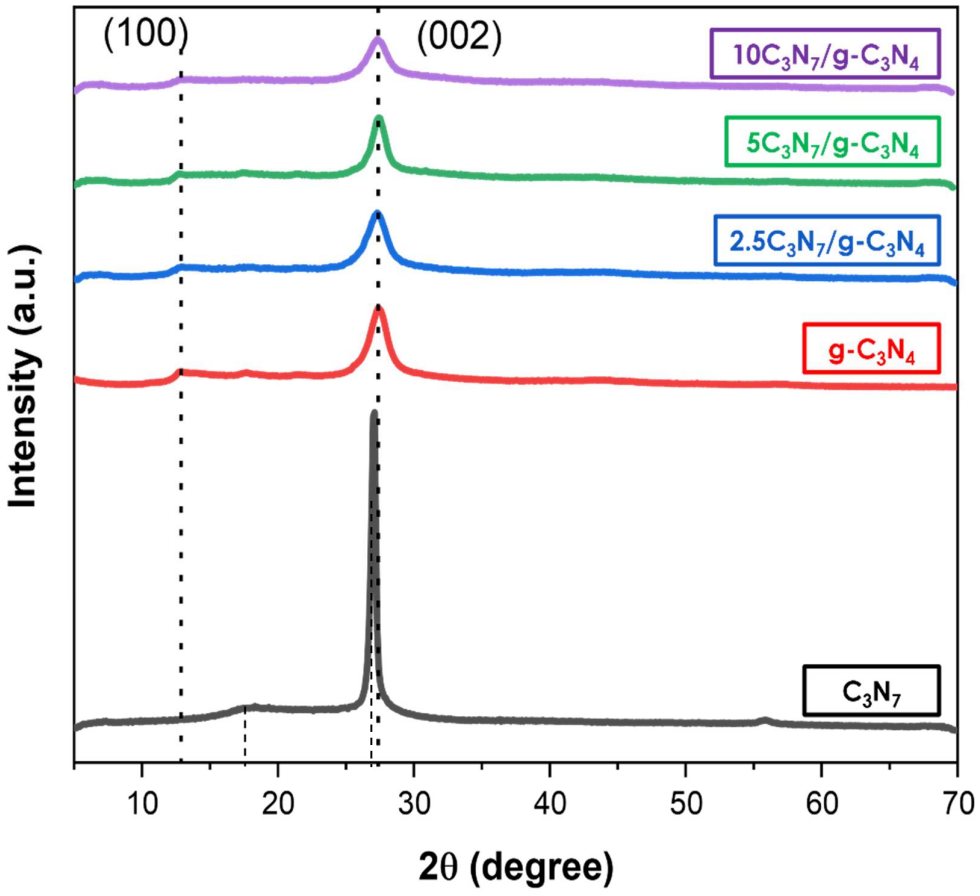

Figure 3.1 Powder X-ray diffraction pattern of g-C_3N_4, C_3N_7 and its composites

The crystalline structure and phase composition of g-C_3N_4, C_3N_7, and their composites were investigated through X-ray diffraction analysis. The pristine g-C_3N_4 displays two distinctive diffraction peaks at 2θ angles of 13° and 27.7°, as depicted in Figure 3.1.[1] The intense peak at 27.7° corresponds to the (002) diffraction plane, indicative of the interlayer stacking of heptazine frameworks. Meanwhile, the smaller peak at 13° is linked to the (100) plane, which arises due to the in-plane periodic arrangement of heptazine units. The

interlayer spacing (d-spacing) corresponding to the 27.7° peak is calculated to be approximately 3.2 Å, reflecting a 2D graphite-like layered configuration.

The diffraction pattern of C_3N_7 similarly features two peaks, one appearing at 27.1°, which is attributed to the (002) plane, and another associated with in-plane structural features. The d-spacing for the (002) plane in C_3N_7 is determined to be 3.33 Å. When compared to g-C_3N_4, the C_3N_7 structure exhibits a slightly increased interlayer distance. The increased spacing may be attributed to electrostatic repulsion between nitrogen atoms. The in-plane d-spacing for C_3N_7 is measured to be 4.9 Å, whereas g-C_3N_4 exhibits a larger in-plane spacing of 6.8 Å. This reduced in-plane spacing in C_3N_7 compared to g-C_3N_4 suggests a structurally distinct core.[2] All synthesized xC_3N_7/g-C_3N_4 composites show diffraction patterns closely resembling those of g-C_3N_4. However, in the composites, the (002) diffraction peak becomes broader and shifts to a lower 2θ value of 27.5°, indicating structural modification. These findings collectively suggest that the crystal structure of the xC_3N_7/g-C_3N_4 composites undergoes noticeable alterations.

3.2 FT-IR (Fourier Transform Infrared) Spectroscopy:

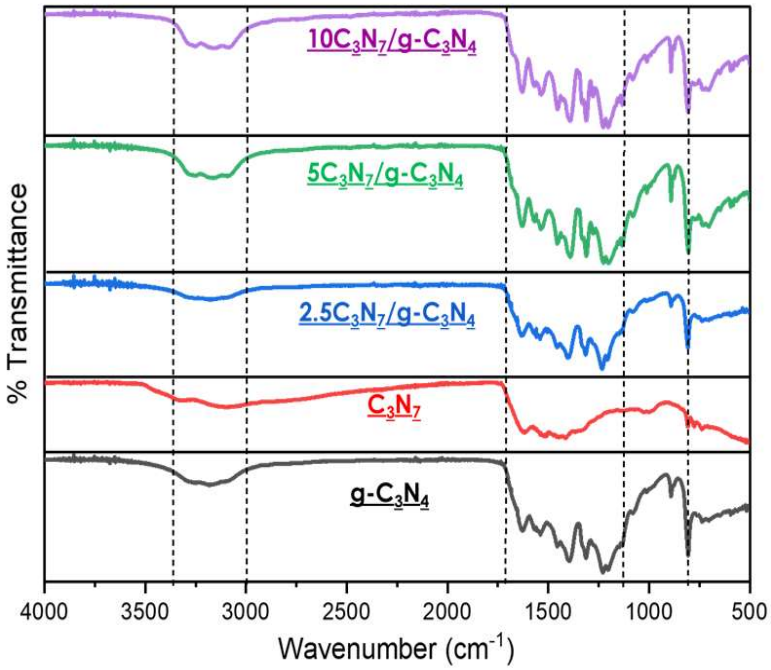

Figure 3.2 Fourier Transform Infrared (FT-IR) Spectrum Analysis of g-C_3N_4, C_3N_7 and its composites.

To understand the functional groups and structural components of the synthesized materials, Fourier Transform Infrared (FT-IR) spectroscopy was conducted. The FT-IR spectrum of pure g-C_3N_4 exhibited characteristic bands around 810, 1200–1700, and 3000–3300 cm^{-1}. These correspond to the out-of-plane breathing mode of the tri-s-triazine ring, C–N stretching vibrations in the heterocyclic structure, and N–H stretching vibrations from residual amino groups, respectively.[4]

In contrast, the FT-IR spectrum of C_3N_7 displayed absorption peaks at 1250, 1335, 1466, 1532, and 1630 cm^{-1}, which are attributed to C–N stretching vibrations within the C_3N_7 heterocyclic framework. Additional peaks at 740 and 780 cm^{-1} indicate the presence of N–N heterocyclic structures, suggesting a core composed of tetrazine or triazole units along with triazine components. Besides the signature 810 cm^{-1} peak typical of tri-s-triazine, C_3N_7 also displayed two more absorption bands at 3150 and 3330 cm^{-1}, associated with standard N–H stretching modes.[2]

The FT-IR spectrum of the all the heterostructures formed revealed all characteristic peaks of g-C_3N_4 and C_3N_7, confirming the coexistence of both g-C_3N_4 and C_3N_7 within the composite material.

3.3 Optical Property and Charge Separation Efficiency:

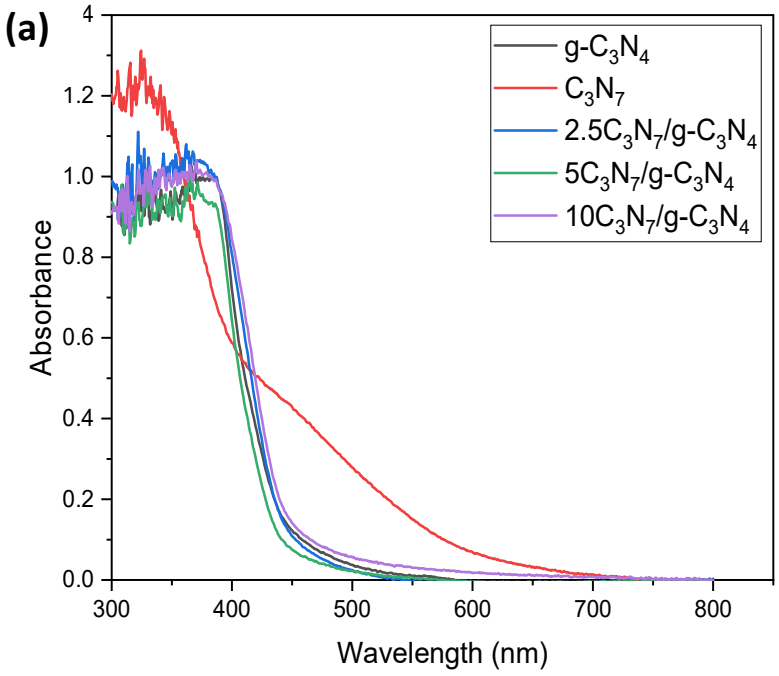

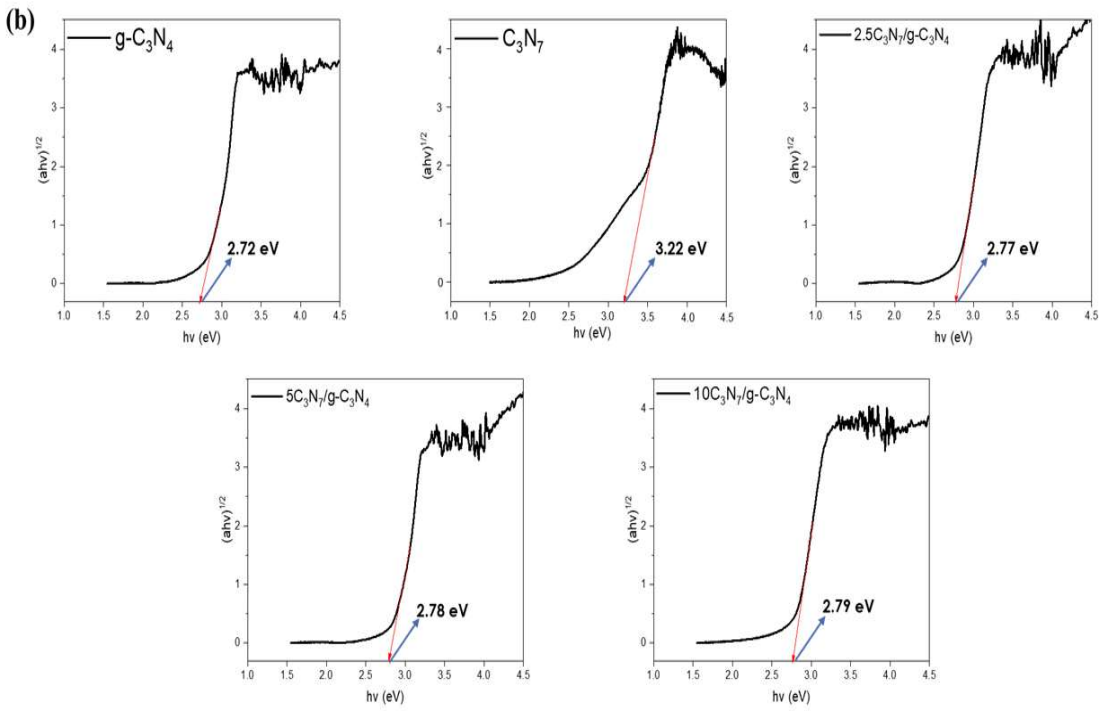

Figure 3.3 (a) UV-Vis DRS Spectrum and (b) Kubelka-Munk plots of as prepared caralysts.

The UV-visible diffuse reflectance spectroscopic (UV-Vis DRS) technique was employed to evaluate the optical characteristics and to estimate the bandgap of the synthesized samples. According to Figure 3.3(a), the pale-yellow g-C_3N_4 material displays significant optical activity within the visible light region, with a major absorption peak around 450 nm, aligning with the visible spectrum range. In contrast, C_3N_7 exhibits an absorption edge at approximately 400 nm. When comparing with g-C_3N_4, all xC_3N_7/g-C_3N_4 composites demonstrate a slight improvement in light absorption. The bandgap values were calculated using the Kubelka-Munk function, as shown in Figure 3.2(b),[3] the estimated bandgap energies for g-C_3N_4 and C_3N_7 are 2.72 eV and 3.22 eV, respectively.

For the composite 2.5C_3N_7/g-C_3N_4, 5C_3N_7/g-C_3N_4, and 10C_3N_7/g-C_3N_4, the bandgaps are consistently around 2.78 eV, indicating that the composite bandgap values fall between those of g-C_3N_4 and C_3N_7.

3.4 Surface Area and Pore Size Distribution:

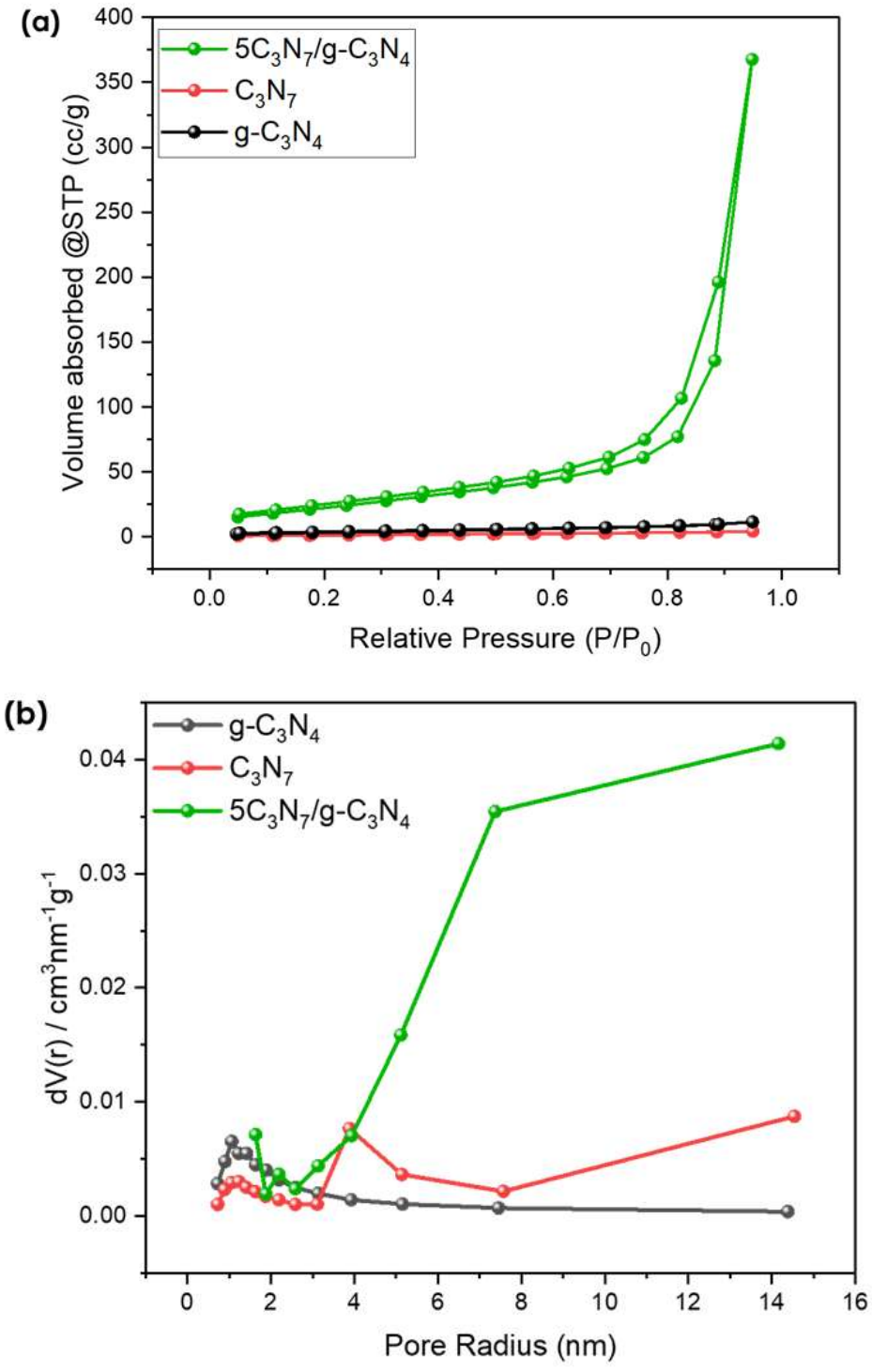

Figure 3.4 (a) N_2 adsorption-desorption isotherm and (b) Pore size distribution of $g\text{-}C_3N_4$, C_3N_7 and $5C_3N_7/g\text{-}C_3N_4$ composite

The specific surface area (SSA) of the synthesized samples was analyzed using the Brunauer–Emmett–Teller (BET) method. The adsorption isotherms of the $5C_3N_7/g\text{-}C_3N_4$ composite displayed (Figure 3.4) a type III hysteresis loop, suggesting a higher adsorption capacity at elevated pressures due to strong interactions between adsorbate molecules after initial adsorption. The measured SSA values were 15.7 m^2/g for $g\text{-}C_3N_4$, 7.0 m^2/g for C_3N_7, and 109.7 m^2/g for the $5C_3N_7/g\text{-}C_3N_4$ composite.

Moreover, the pore radius of the composite significantly expanded to 14.15 nm, while $g\text{-}C_3N_4$ showed a smaller pore radius of 1.06 nm. This substantial increase in surface area and pore size for the $5C_3N_7/g\text{-}C_3N_4$ composite can be attributed to the arrangement of carbon nitride (CN) layers, which enhances the accessibility of active sites and adsorption efficiency. Additionally, the pore volume of the composite (0.58 cm^3/g) was much higher than that of the individual $g\text{-}C_3N_4$ and C_3N_7 samples.

These enhancements in surface area, pore radius, and pore volume collectively contribute to improved photocatalytic performance. As a result, the $5C_3N_7/g\text{-}C_3N_4$ composite demonstrates significant potential for adsorption-based applications and shows excellent photocatalytic activity.

Table 3.1 Textural Parameters of $g\text{-}C_3N_4$, C_3N_7 and $5C_3N_7/g\text{-}C_3N_4$ composite.

Sample	Surface Area (m^2g^{-1})	Pore Radius (nm)	Pore Volume (cm^3g^{-1})
$g\text{-}C_3N_4$	15.7	1.06	0.018
C_3N_7	7	1.23	0.007
$5C_3N_7/g\text{-}C_3N_4$	109.7	14.15	0.58

3.5 SEM Images:

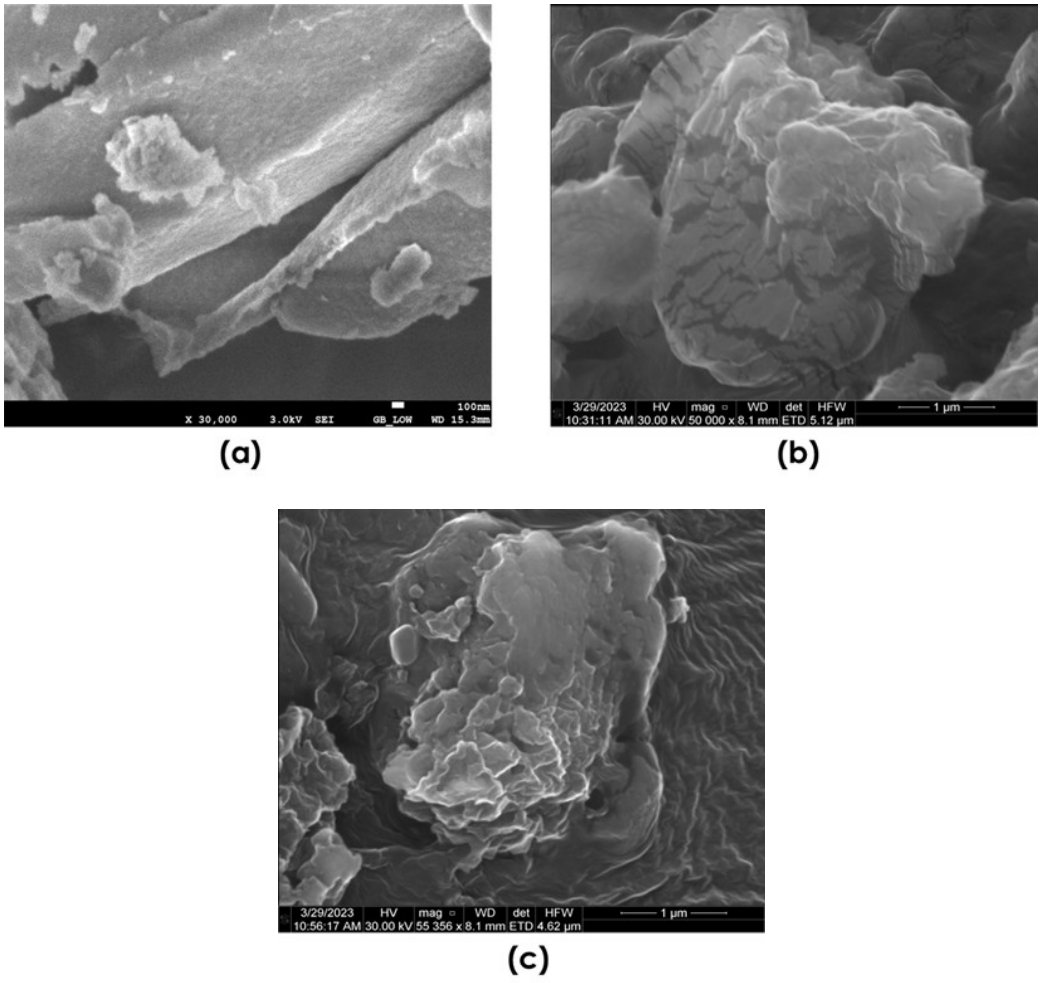
X 30,000 3.0kV SEI GB_LOW WD 15.3mm 100nm
(a)
3/29/2023 HV mag WD det HFW 1 µm
10:31:11 AM 30.00 kV 50 000 x 8.1 mm ETD 5.12 µm
(b)
3/29/2023 HV mag WD det HFW 1 µm
10:56:17 AM 30.00 kV 55 356 x 8.1 mm ETD 4.62 µm
(c)

Figure 3.5 SEM Images of (a) g-C_3N_4, (b) C_3N_7, and (c) 5C_3N_7/g-C_3N_4

Scanning Electron Microscopy (SEM) was used to observe the surface structures of g-C_3N_4, C_3N_7, and their composite 5C_3N_7/g-C_3N_4.

The SEM image of **g-C_3N_4,** Figure 3.5(a) shows thin, layered sheet-like structures. These layers resemble stacked paper and are typical of graphitic carbon nitride. The smooth and flat surfaces suggest that the material has a relatively low surface roughness, which could limit how many active sites are available for photocatalytic reactions.

In the case of **C_3N_7,** Figure 3.5(b), the structure is more irregular and has a flower-like appearance. The surface is rough and made up of many folds and wrinkles. This rough texture increases the surface area, which may improve the material's ability to interact with light and other molecules during reactions.

The **5C_3N_7/g-C_3N_4 composite**, Figure 3.5(c) appears as the sheet-like layers of g-C_3N_4 and bulkier C_3N_7 particles. This suggests that C_3N_7 has been successfully loaded onto the g-C_3N_4 surface and it has increase light absorption and improve charge separation during photocatalysis.

3.6 TEM Images:

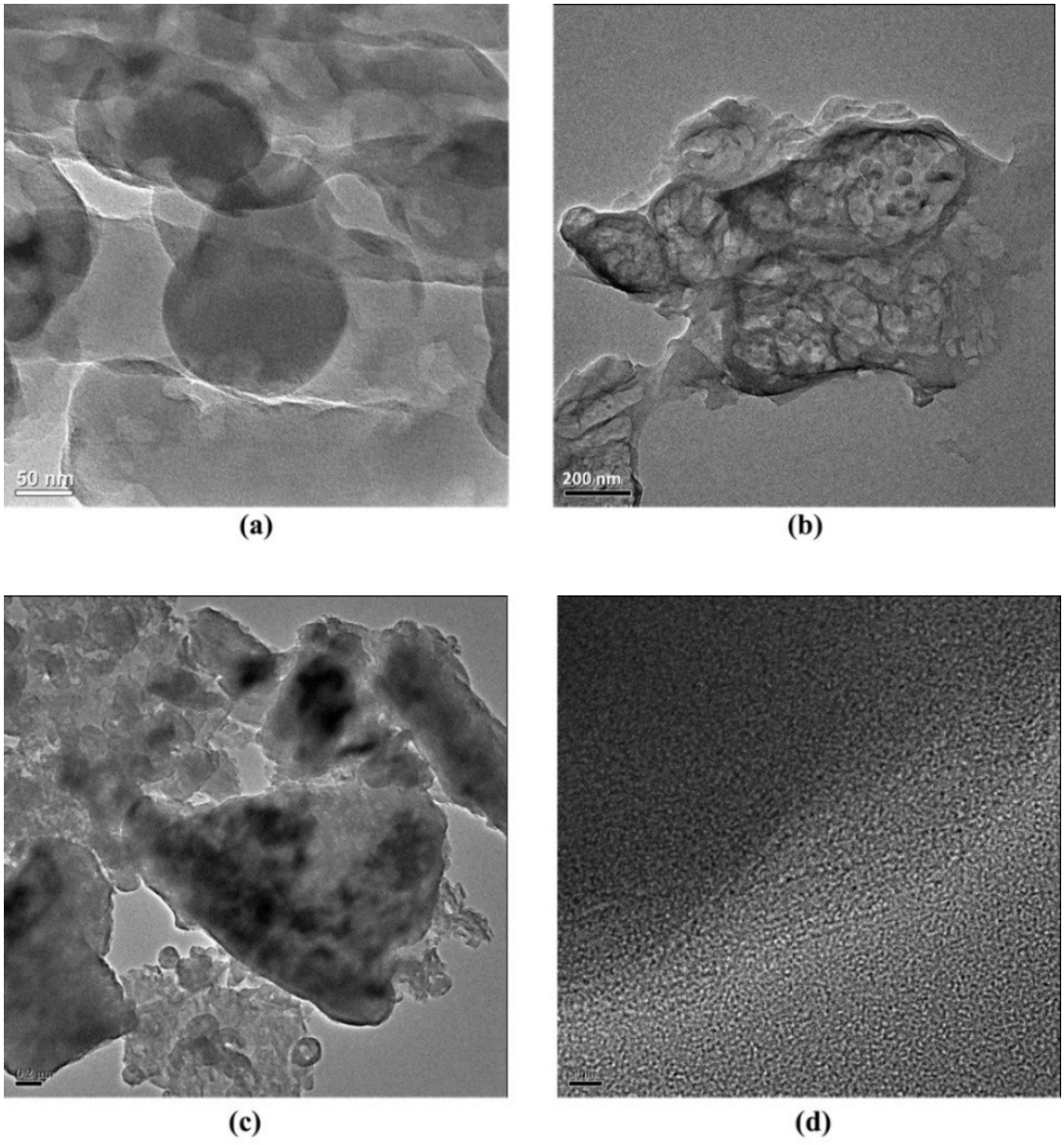

Figure 3.6 TEM and HR-TEM images of (a) g-C_3N_4, (b) C_3N_7, (c) and (d) 5C_3N_7/g-C_3N_4

Transmission electron microscopy (TEM) was employed to investigate the microstructural characteristics of the C_3N_7/g-C_3N_4 composite. The sheet-like morphology is indicative of the layered structure typical of graphitic carbon nitride (g-C_3N_4) as shown in image (a), while the irregular and less-defined regions are attributed to the C_3N_7 component as shown in Figure 3.6(b). The low-magnification TEM Figure 3.6(c) reveals a heterogeneous assembly of agglomerated nanosheets and amorphous domains. These features suggest an intimate mixing of the two constituents, forming a hybrid structure.

The presence of ultrathin layers and partial transparency in several regions supports the nanoscale thickness of the sheets, enhancing surface area and potentially improving photocatalytic activity by providing more active sites for redox reactions.

High-resolution TEM (HRTEM) imaging in Figure 3.6(d) offers further insights into the crystallographic features. The image displays a uniform contrast with no well-defined lattice fringes, which is consistent with the amorphous or poorly crystalline nature of the 5C_3N_7/g-C_3N_4 composite.

3.7 Evaluation of Photocatalytic Degradation Behaviour and Mechanism:

The photocatalytic capabilities of g-C_3N_4, C_3N_7, and their synthesized composites (xC_3N_7/g-C_3N_4) were studied for degradation of Rhodamine B dye (30 mg/L).

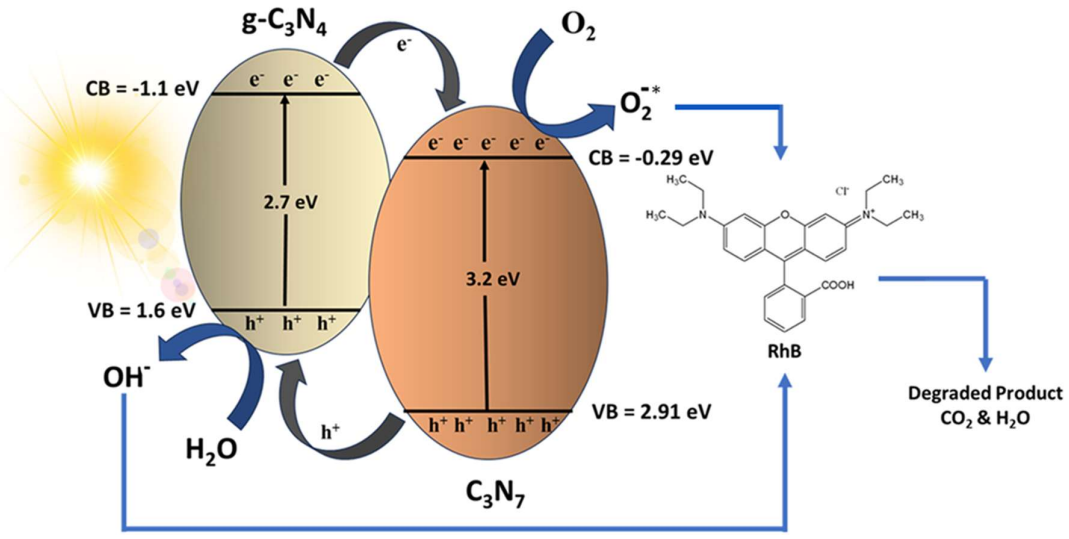

Figure 3.7 Plausible Mechanism for photodegradation of RhB

3.7.1 Photocatalytic Rhodamine B Degradation:

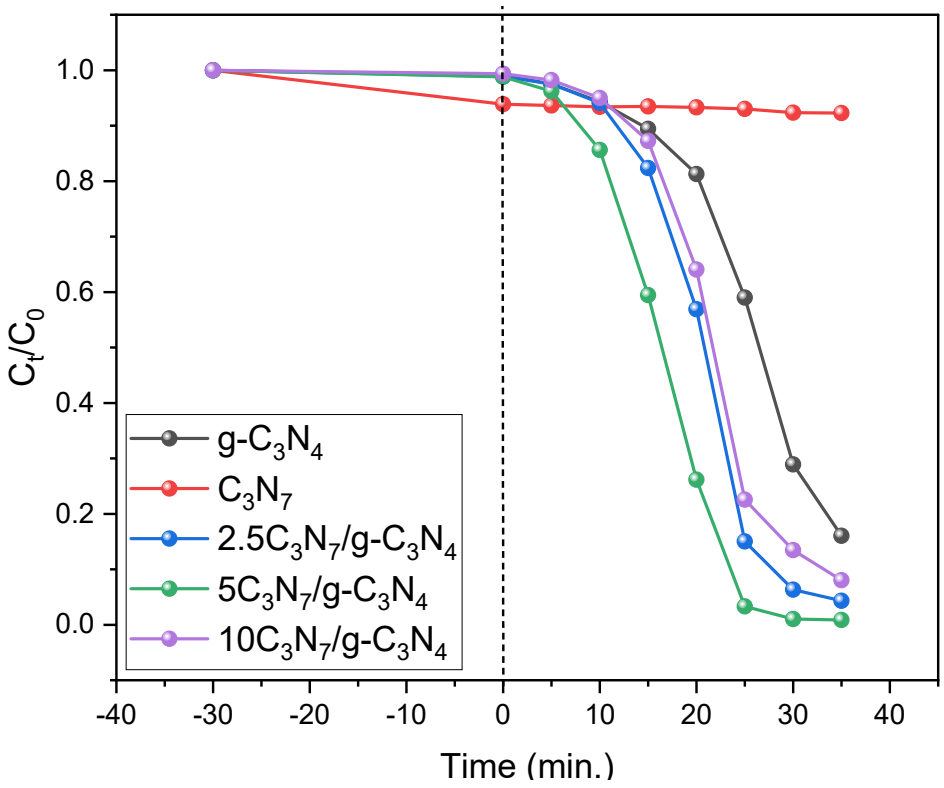

Figure 3.8 Photocatalytic RhB (30 mg/L) degradation performance of g-C_3N_4, C_3N_7 and its composites.

The photocatalytic degradation of Rhodamine B (RhB) dye was carried out using the same photocatalytic reactor setup described earlier. In this experiment, 50 mg of catalyst was added to 50 mL of a 30 mg·L^{-1} RhB solution. To ensure equilibrium between the catalyst and dye molecules, the mixture was kept in the dark for 30 minutes to allow adsorption-desorption balance before light exposure. During irradiation, samples were collected at 5-minute intervals to track changes in RhB concentration. After centrifugation, the samples were analysed using a UV-Vis spectrophotometer (UV-1800 Shimadzu) to measure absorbance. After 35 minutes of light exposure, approximately 70% of the RhB was degraded when g-C_3N_4 was used as the catalyst (Figure 3.8). In contrast, the 5C_3N_7/g-C_3N_4 composite exhibited the highest degradation efficiency, achieving 95%, outperforming both the individual g-C_3N_4 and other C_3N_7/g-C_3N_4 composites.

Control experiments conducted in dark conditions and without the catalyst (photolysis) confirmed that both light and the photocatalyst are essential and work together effectively to enhance RhB degradation.

3.7.1.1 Quenchers Study:

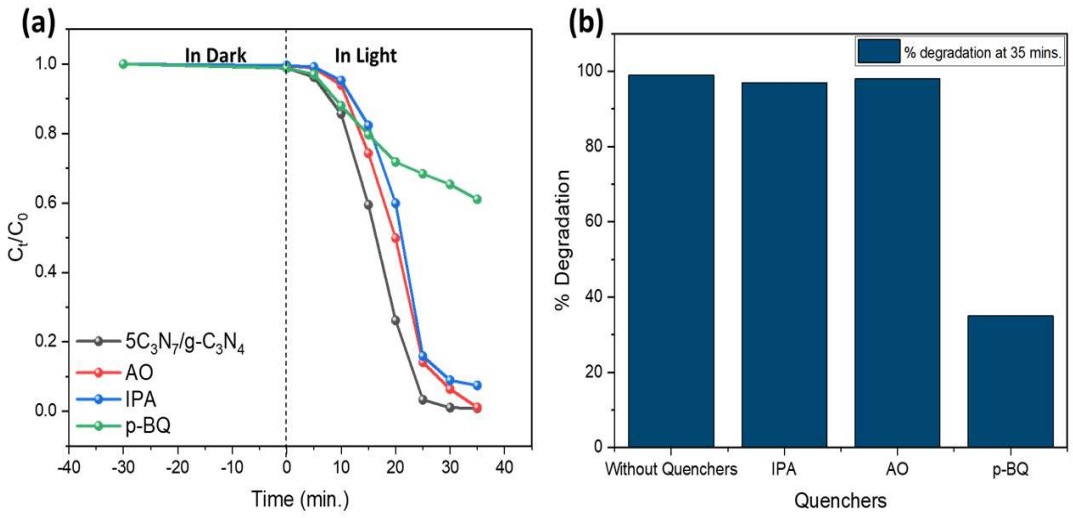

Figure 3.9 (a) Photocatalytic Dye Degradation by $5C_3N_7/g\text{-}C_3N_4$ in presence of scavengers, and (b) Corresponding Percentage Degradation in presence of quenchers.

To better understand the degradation mechanism of Rhodamine B (RhB), a series of quenching experiments were conducted using the photocatalyst $5C_3N_7/g\text{-}C_3N_4$. These tests involved the use of specific scavengers to isolate and identify the reactive oxidative species (ROS) involved in the photodegradation process. Isopropanol (IPA), ammonium oxalate (AO), and para-benzoquinone (p-BQ) were utilized to trap hydroxyl radicals ($OH^{\bullet}$), photogenerated holes (h^{+}), and superoxide radicals ($O_2^{-\bullet}$), respectively.

The findings showed that the presence of AO had little to no effect on the degradation efficiency, suggesting that holes do not significantly contribute to the degradation of RhB. Conversely, when IPA was introduced, a slight reduction in photocatalytic activity was observed, indicating the participation of hydroxyl radicals ($OH^{\bullet}$). Notably, the introduction of p-BQ resulted in a substantial decrease in degradation performance, highlighting the key role of superoxide radicals ($O_2^{-\bullet}$) in the photodegradation of RhB dye.

These results collectively demonstrate that among the reactive species tested, ($O_2^{-\bullet}$) plays the most critical role in the degradation process, followed by ($OH^{\bullet}$), while (h^+) has minimal impact under the given experimental conditions.

3.7.1.2 Recyclability:

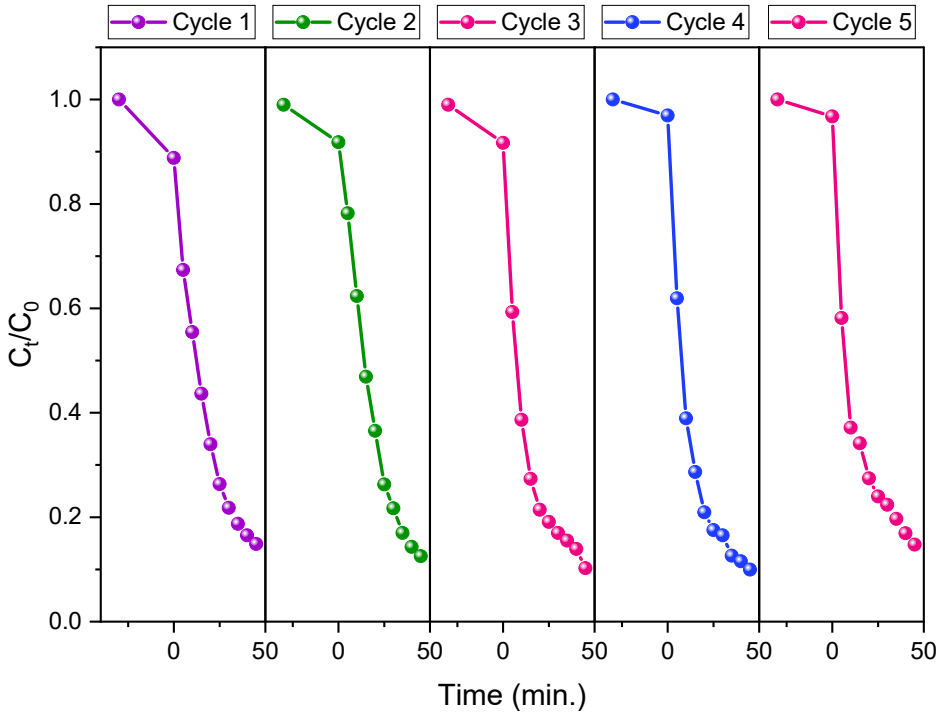

Figure 3.10 Recyclability assessment of 5C_3N_7/g-C_3N_4 catalyst for degradation of RhB

To evaluate the reusability of the 5C_3N_7/g-C_3N_4 catalyst as shown in Figure 3.10 it was tested using an aqueous RhB (30 mg/L). After each photocatalytic degradation of RhB (30 mg/L). The catalyst was separated by centrifugation washed with water and acetone, dried and reused for the next experiment. Five cycles of the photocatalytic degradation of RhB (30 mg/L) was perform and results are shown in Figure 3.10. The results demonstrate that the catalyst maintains its performance over five consecutive cycles, as shown in Figure 3.10, with no significant decline in degradation efficiency observed after the fifth cycle.

3.8 Photocatalytic Reduction of Cr(VI) to Cr(III):

The Figure 3.11 shows the photocatalytic reduction of Cr(VI) to Cr(III) over time using different photocatalysts under exposure to visible light. Pristine g-C_3N_4 shows moderate reduction of Cr(VI), with about 20% remaining after 35 minutes. C_3N_7 performs poorly with the least Cr(VI) reduction (~40% Cr(VI) still present at 35 minutes). All composite materials xC_3N_7/g-C_3N_4 outperform both pure g-C_3N_4 and C_3N_7. 5C_3N_7/g-C_3N_4 shows the best performance with nearly complete reduction of Cr(VI) within 35 minutes. 2.5C_3N_7/g-C_3N_4 and 10C_3N_7/g-C_3N_4 also perform very well, indicating a synergistic effect in the composites.

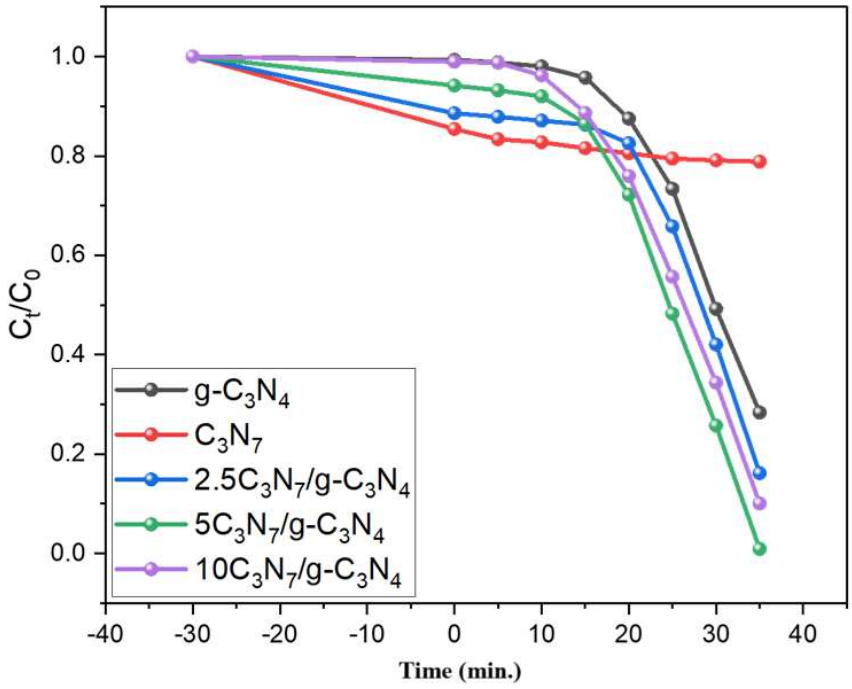

Figure 3.11 Photocatalytic reduction of Cr(VI) to Cr(III)

3.9 References:

1 Bhoyar, T.; Kim, D. J.; Abraham, B. M.; Tonda, S.; Manwar, N. R.; Vidyasagar, D.; Umare, S., Tailoring photoactivity of polymeric carbon nitride via donor-π-acceptor network. Applied Catalysis B: Environmental **2022**, 310, 121347.

2 Kim, I. Y.; Kim, S.; Premkumar, S.; Yang, J. H.; Umapathy, S.; Vinu, A., Thermodynamically stable mesoporous C3N7 and C3N6 with ordered structure and their excellent performance for oxygen reduction reaction. Small **2020**, 16 (12), 1903572.

3 Bott-Neto, J. L.; Martins, T. S.; Buscaglia, L. A.; Machado, S. A.; Oliveira Jr, O. N., Photocatalysis of TiO2 Sensitized with Graphitic Carbon Nitride and Electrodeposited Aryl Diazonium on Screen-Printed Electrodes to Detect Prostate Specific Antigen under Visible Light. ACS Applied Materials & Interfaces **2022**, 14 (19), 22114-22121.

4 Dong, F.; Li, Y.; Wang, Z.; Ho, W.-K., Enhanced visible light photocatalytic activity and oxidation ability of porous graphene-like g-C3N4 nanosheets via thermal exfoliation. Applied Surface Science **2015**, 358, 393-403.

5 Liu, C.; Dai, H.; Tan, C.; Pan, Q.; Hu, F.; Peng, X., Photo-Fenton degradation of tetracycline over Z-scheme Fe-g-C3N4/Bi2WO6 heterojunctions: Mechanism insight, degradation pathways and DFT calculation. Applied Catalysis B: Environmental **2022**, 310, 121326.

6 Bhoyar, T.; Saraswat, N.; Jyothirmai, M.; Gupta, A.; Malla, S. K.; Park, J.; Vidyasagar, D.; Umare, S. S., Nitrogen-Doped Graphitic Carbon Dots Embedded in Carbon Nitride Scaffolds for Water Decontamination. ACS Applied Nano Materials **2023**, 6 (5), 3484-3496.

CHAPTER 4

SUMMARY AND CONCLUSION

4.1 Summary and Conclusion:

Photocatalysis offers significant capability in supporting energy and environmental innovations. Utilizing g-C_3N_4 as a photocatalyst enables the transformation of harmful waste materials into environmentally friendly, non-toxic compounds. However, despite its advantages, g-C_3N_4 has certain limitations that hinder its overall efficiency. To address these shortcomings, a heterostructure was developed by integrating g-C_3N_4 with a nitrogen-rich material known as C_3N_7. The resulting synthesis of the composites (xC_3N_7/g-C_3N_4) were achieved by the means of a straightforward thermal polymerization technique.

Compared to pure g-C_3N_4, the newly formed composites showed notable improvements in their physical properties. These enhancements translated into superior photocatalytic performance, particularly in degrading the antibiotic tetracycline hydrochloride (TCH) and the dye Rhodamine B (RhB) under visible light. Among the variations, the 5C_3N_7/g-C_3N_4 composite demonstrated the most efficient degradation capabilities. This performance is linked to its enhanced ability to separate charge carriers, prolonged charge carrier lifespan, and increased surface area all of which contributed to its superior photocatalytic behaviour.

Quenching experiments revealed that the presence of $O_2^{\bullet-}$ radicals played a very important role in the degradation of both TCH and RhB. The overall findings emphasize the effectiveness of using C_3N_7 to construct a metal-free composite that significantly boosts the photocatalytic activity of g-C_3N_4.

4.2 Future Aspects:

Future investigations will delve into more advanced characterization techniques to better understand and enhance interfacial interactions within the composites. Additionally, the 5C_3N_7/g-C_3N_4 composite shows promise for broader applications, such as hydrogen production via water splitting, and generation of hydrogen peroxide (H_2O_2), among others.